

## RESEARCH ARTICLE

# Molecular precursor pathway to $\text{Co}_{1-x}\text{Ni}_x\text{Nb}_2\text{O}_6$ for photocatalytic dye degradation: Optical and charge transport studies

Ana Lozančić | Martina Vrankić | Marta Razum | Luka Pavić |

Lidija Androš Dubraja  | Marijana Jurić 

Ruder Bošković Institute, Zagreb, Croatia

## Correspondence

Marijana Jurić, Ruder Bošković Institute,  
Bijenička cesta 54, 10000, Zagreb, Croatia.  
Email: [Marijana.Juric@irb.hr](mailto:Marijana.Juric@irb.hr)

## Funding information

Croatian Science Foundation,  
Grant/Award Number: IP-2019-04-5742;  
European Union from the European  
Regional Development Fund,  
Grant/Award Number: KK.01.1.1.11.0001

## Abstract

A new approach for the formation of binary and ternary mixed metal oxides, namely,  $\text{CoNb}_2\text{O}_6$ ,  $\text{NiNb}_2\text{O}_6$ , and  $\text{Co}_{0.5}\text{Ni}_{0.5}\text{Nb}_2\text{O}_6$ , through a modified single-source molecular precursor route was investigated. By optimizing the annealing temperature, heating/cooling rates and holding times, the phase compositions of thermal processing of mixtures of oxalate-based complexes  $[\text{M}(\text{bpy})_3]_2[\text{NbO}(\text{C}_2\text{O}_4)_3]\text{Cl}\cdot n\text{H}_2\text{O}$  ( $\text{M} = \text{Co}^{2+}$  (1) or/and  $\text{Ni}^{2+}$  (2);  $n = 11, 12$ ) and  $(\text{NH}_4)_3[\text{NbO}(\text{C}_2\text{O}_4)_3]\cdot 3\text{H}_2\text{O}$  (3) were evaluated. Phase-pure columbite oxides  $\text{Co}_{1-x}\text{Ni}_x\text{Nb}_2\text{O}_6$  ( $x = 0, 0.5, \text{ and } 1$ ) were obtained in one step by heating the mixtures of two (1 and 3, or 2 and 3) or three oxalate complexes (1 and 2 and 3) at  $1200^\circ\text{C}$  for 10 h with a heating/cooling rate of  $10^\circ\text{C min}^{-1}$ . The (micro)structure, morphology, and optical properties of the as-prepared materials were characterized by powder X-ray diffraction (PXRD), field-emission scanning electron microscopy (FE-SEM) and ultraviolet–visible diffuse reflectance spectroscopy (UV–Vis DRS). Impedance spectroscopy was used to investigate the electrical and dielectric properties, providing valuable insights into the charge transport dynamics. The  $\text{CoNb}_2\text{O}_6$  exhibits the greatest conductivity in the series ( $2.64 \times 10^{-11} \Omega^{-1} \text{cm}^{-1}$  at  $120^\circ\text{C}$ ), two orders of magnitude greater than those of  $\text{NiNb}_2\text{O}_6$  and  $\text{Co}_{0.5}\text{Ni}_{0.5}\text{Nb}_2\text{O}_6$ . The ternary oxide  $\text{Co}_{0.5}\text{Ni}_{0.5}\text{Nb}_2\text{O}_6$  has a minimum in conductivity and dielectric loss, but it shows a maximum in dielectric permittivity. Estimated band gap energies of  $\text{CoNb}_2\text{O}_6$ ,  $\text{NiNb}_2\text{O}_6$ , and  $\text{Co}_{0.5}\text{Ni}_{0.5}\text{Nb}_2\text{O}_6$  within the visible light excitations prompt us to investigate their photocatalytic activities in the degradation of the methylene blue (MB) dye under visible light irradiation without and with hydrogen peroxide ( $\text{H}_2\text{O}_2$ ). It is evident that the  $\text{Co}_{1-x}\text{Ni}_x\text{Nb}_2\text{O}_6/\text{H}_2\text{O}_2$  systems exhibit higher photocatalytic activity: the degradation efficiency of MB was found to be between 26% and 38%. In addition, the cyclic stability

This is an open access article under the terms of the [Creative Commons Attribution-NonCommercial-NoDerivs](https://creativecommons.org/licenses/by-nc-nd/4.0/) License, which permits use and distribution in any medium, provided the original work is properly cited, the use is non-commercial and no modifications or adaptations are made.

© 2025 The Author(s). Journal of the American Ceramic Society published by Wiley Periodicals LLC on behalf of American Ceramic Society.

of the photocatalyst was investigated and a possible proposed photocatalytic degradation mechanism was substantiated by a scavenger analysis study.

#### KEYWORDS

columbite niobate-based oxides, electrical properties, (micro)structural characterization, molecular precursors, photocatalytic activity

## 1 | INTRODUCTION

The properties of mixed metal oxides, an important class of advanced materials, can be strongly influenced by crystallinity, particle size, phases present, and morphology. These can be partially adjusted by altering the synthesis methods.<sup>1–7</sup> A conventional way for producing oxide materials is based on the solid-state reactions using oxide, carbonate, or nitrate precursors. This method requires a heat treatment at relatively high temperatures, as well as long-term and repetitive grinding processes. It often yields low-purity products with a multiphase composition comprising leftover reactants. A complete control over the particle size and shape is also a prerequisite for the photocatalytic applications of oxide materials, where a high surface area, which enhances substrate adsorption and increases the number of active sites, is considered essential. However, the high-temperature treatments are generally used for the synthesis of highly crystalline materials, which frequently result in increased particle size, and consequently, in decreased surface area. Therefore, achieving both high crystallinity and high surface area in a one-step synthesis remains difficult.<sup>8–11</sup>

Due to these limitations, the use of heterometallic systems as single-source precursors has provided alternative synthetic route to mixed metal oxides obtained by reconstructing the molecular bonding topology and removing the supporting organic groups via thermal decomposition. It has been observed that using a well-defined precursor can result in a crystalline oxide materials under conditions that are much milder than those utilized in traditional solid-state synthesis. The advantage of a solid phase transition is the retention of the elemental composition defined by the molecular precursor while losing only volatile decomposition products, allowing for the superior stoichiometric control of the intermetallic ratio in the oxide products. The final products are the homogeneous due to the mixing of the metals at the molecular level. In addition, the presence of bridging or chelating ligands in the precursors prevents metal separation during oxide formation.<sup>8–12</sup> The decomposition of metal–organic species requires the release of gaseous organic decomposition products (and possibly solvent molecules), which might influence the particle size and porosity of the result-

ing oxide. A larger organic content in the starting materials allows for greater porosity and smaller particle sizes in the decomposition products, owing to increased gas release during thermolysis.

The *single-source precursor* method is an essential *soft chemistry* approach for the preparation of oxides in the form of nanosized particles and thin films.<sup>13–16</sup> A proper selection of ligands is required for successful *molecular precursor-to-material* conversion. The nature of the ligand used provides the precursor with a clean, low-temperature thermolysis that results in a phase-pure target material. Importantly, the low cost of the ligand makes heterometallic precursors highly attractive to industrial applications.<sup>15–17</sup> The oxalate dianion,  $C_2O_4^{2-}$ , is a suitable ligand for the synthesis of molecular precursors for oxides because it decomposes easily on gaseous  $CO_2$  and  $CO$  at moderate temperatures. This ligand also has the benefit of being widely available and inexpensive.<sup>18</sup> Several studies have shown that heterometallic oxalate complexes may be employed as suitable precursors for the preparation of mixed-metal oxides.<sup>18–30</sup>

Metal–organic complexes may not always have the appropriate stoichiometry to be used as molecular precursors for the thermal degradation to produce the desired single-phase oxide materials in a single step. Furthermore, the preparation of the coordination compound with two or more different metals in a suitable ratio and properly coordinated ligand is a challenging task. Therefore, by mixing two or more adequate precursors in the proper ratio prior to thermal treatment, an oxide containing two or more metals might be formed. For example, the binary oxide  $BiVO_4$  can be formed by direct pyrolysis of  $BiV(O)(Hsal)(sal)(salen^*)\cdot CH_2Cl_2$  [ $sal = O_2CC_6H_4-2-O$ ;  $Hsal = O_2CC_6H_4-2-OH$ ;  $salen^* = ethylenebis(3-methoxysalicylimine)$ ], while the heat treatment of mixtures of  $BiV(O)(Hsal)(sal)(salen^*)\cdot CH_2Cl_2$  and  $BiCu(Hsal)_3(salen)$  or  $BiNi(Hsal)_3(salen)\cdot CH_2Cl_2$  [ $salen = ethylenebis(salicylimine)$ ] results in isolation of the ternary oxide  $Bi_2V_xM_{1-x}O_{5.5-\delta}$  ( $M = Cu, Ni$ ).<sup>31</sup>

The columbite niobate-based oxides are a class of materials with compelling optical, dielectric, magnetic and catalytic properties. The  $MNb_2O_6$  ( $M = Co$  and  $Ni$ ) niobates exhibit quasi-one-dimensional magnetic properties. The magnetic ordering is generally observed at

relatively low temperatures (usually below 10 K), and all ordered phases are antiferromagnetic.<sup>32–37</sup> These oxides typically have a high dielectric constant and low dielectric losses at microwave frequencies making them suitable as dielectric resonators and filters for use in mobile and satellite communications. In addition, the  $\text{CoNb}_2\text{O}_6$  and  $\text{NiNb}_2\text{O}_6$  have attracted much attention as anode materials for lithium-ion batteries due to their excellent fast-charging capability.<sup>38–40</sup> Furthermore, the photoluminescence of  $\text{NiNb}_2\text{O}_6$  nanoparticles showed a blue emission at 440 nm due to the distorted edge-shared  $\text{NbO}_6$  groups,<sup>41</sup> and its estimated band gap was 2.2 eV, so it could be tested as a solid photocatalyst for a water splitting.<sup>35,42</sup>

The synthesis of niobate-based oxides usually requires high temperatures above 1100°C or a complex chemical process. Therefore, there are different methods for the production of  $\text{MNb}_2\text{O}_6$  ( $M = \text{Co}$  and  $\text{Ni}$ ) materials. The most widely used method is traditional solid-state reaction, in which stoichiometric amounts of  $\text{Nb}_2\text{O}_5$  and metal elements or oxides are heated to high temperatures to synthesize polycrystalline powders.<sup>35–38,40,42</sup> The  $\text{NiNb}_2\text{O}_6$  nanoparticles were also synthesized by a sol-gel combustion method using citric acid as fuel and nitrates as oxidants at a relatively low temperature compared to the solid-state reaction method.<sup>41</sup> In addition,  $\text{CoNb}_2\text{O}_6$  and  $\text{NiNb}_2\text{O}_6$  ceramics were successfully synthesized by a coprecipitation technique or by a few-step hydrothermal process followed by heat treatment.<sup>32,43,44</sup> Furthermore, the  $\text{CoNb}_2\text{O}_6$  with rutile structure was prepared by hydrothermal synthesis using polyvinyl alcohol as an additive.<sup>45</sup> In general, the precursor route has advantages and disadvantages compared to the sol-gel method, which is based on a low-temperature process using a solution of a metal alkoxide that forms a gel after hydrolysis and condensation at room temperature (RT). This liquid-phase method is a cost-effective and environmentally friendly for producing nanocomposites, as it allows good control of microstructure, particle size, dispersion, structure, and chemical composition by carefully monitoring the preparation parameters. To obtain pure and crystalline materials, these processes usually require further steps such as washing, calcination, and postheating. The main disadvantage compared to the precursor route for obtaining oxide materials is therefore the limited efficiency and the long duration of the synthesis process.<sup>5,41,46,47</sup> The use of a heterometallic compound as a molecular precursor is usually only one of the functionalities investigated for the precursor compound. The metal oxide is obtained in a one step and without repeated heating and grinding processes, but generally at higher temperatures.

In this work, we have investigated the feasibility of combining the molecular precursor route and

solid-state reaction to synthesize the oxide materials  $\text{CoNb}_2\text{O}_6$ ,  $\text{NiNb}_2\text{O}_6$ , and  $\text{Co}_{0.5}\text{Ni}_{0.5}\text{Nb}_2\text{O}_6$ . The synthesis process involves mixing the oxalate precursors  $[\text{M}(\text{bpy})_3]_2[\text{NbO}(\text{C}_2\text{O}_4)_3]\text{Cl}\cdot n\text{H}_2\text{O}$  (where  $M = \text{Co}^{2+}$  or/and  $\text{Ni}^{2+}$  and  $n = 11, 12$ )<sup>48</sup> and  $(\text{NH}_4)_3[\text{NbO}(\text{C}_2\text{O}_4)_3]\cdot 3\text{H}_2\text{O}$ <sup>25</sup> in appropriate ratios. By optimizing the annealing temperature, heating/cooling rates and holding times, the single-phase oxide material was obtained. The phase formation, structural arrangement and morphological versatility of these multimetallic oxides were characterized by powder X-ray diffraction (PXRD) and field-emission scanning electron microscopy (FE-SEM). Furthermore, the optical and detailed electrical properties of the resulting oxide phases were investigated by ultraviolet–visible diffuse reflectance spectroscopy (UV–Vis DRS) and impedance spectroscopy. Additionally, the photocatalytic activity in the degradation of the methylene blue (MB) dye pollutant under visible light irradiation was assessed.

Due to the attractive properties and promising applications of  $\text{CoNb}_2\text{O}_6$  and  $\text{NiNb}_2\text{O}_6$ , it is intriguing and demanding to investigate unique synthetic approach to produce these oxides. The properties of ternary columbite  $\text{Co}_{0.5}\text{Ni}_{0.5}\text{Nb}_2\text{O}_6$  have also not yet been investigated or reported. Furthermore, we have investigated the impact of modified molecular precursor route on the structure, as well as the electrical and photocatalytic characteristics of the  $\text{Co}_{1-x}\text{Ni}_x\text{Nb}_2\text{O}_6$  ( $x = 0, 0.5$ , and 1).

## 2 | EXPERIMENTAL SECTION

### 2.1 | Materials

All used chemicals were purchased from commercial sources and used without further purification. The  $[\text{M}(\text{bpy})_3]_2[\text{NbO}(\text{C}_2\text{O}_4)_3]\text{Cl}\cdot n\text{H}_2\text{O}$  [ $M = \text{Co}^{2+}$  (1) and  $\text{Ni}^{2+}$  (2);  $n = 11, 12$ ] and  $(\text{NH}_4)_3[\text{NbO}(\text{C}_2\text{O}_4)_3]\cdot 3\text{H}_2\text{O}$  (3) were prepared according to previously described procedures.<sup>25,48</sup>

### 2.2 | Thermal synthesis of $\text{Co}_{1-x}\text{Ni}_x\text{Nb}_2\text{O}_6$ ( $x = 0, 0.5$ , and 1)

Crystals of  $[\text{Co}(\text{bpy})_3]_2[\text{NbO}(\text{C}_2\text{O}_4)_3]\text{Cl}\cdot n\text{H}_2\text{O}$  (1) and  $(\text{NH}_4)_3[\text{NbO}(\text{C}_2\text{O}_4)_3]\cdot 3\text{H}_2\text{O}$  (3), of  $[\text{Ni}(\text{bpy})_3]_2[\text{NbO}(\text{C}_2\text{O}_4)_3]\text{Cl}\cdot n\text{H}_2\text{O}$  (2) and  $(\text{NH}_4)_3[\text{NbO}(\text{C}_2\text{O}_4)_3]\cdot 3\text{H}_2\text{O}$  (3), and those of  $[\text{Co}(\text{bpy})_3]_2[\text{NbO}(\text{C}_2\text{O}_4)_3]\text{Cl}\cdot n\text{H}_2\text{O}$  (1),  $[\text{Ni}(\text{bpy})_3]_2[\text{NbO}(\text{C}_2\text{O}_4)_3]\text{Cl}\cdot n\text{H}_2\text{O}$  (2), and  $(\text{NH}_4)_3[\text{NbO}(\text{C}_2\text{O}_4)_3]\cdot 3\text{H}_2\text{O}$  (3) were mixed in the proper ratios (1:3, 1:3, and 1:1:6, respectively) prior to thermal decomposition. Finely ground crystalline

powders were heated in a furnace (Nabertherm, Model LHT 02/16) in a Pt crucible from room temperature (RT) to a temperature range of 600–1300°C in air, at a rate of 5 and 10°C min<sup>-1</sup> and then cooled to RT in the same way. At specific temperatures, selected samples were held for several hours (6, 10, 18, or 24). After thermal treatment, the resulting oxides were characterized by PXRD at RT.

### 2.3 | Powder X-ray diffraction measurements

The PXRD data were collected in a reflection mode with monochromatic Cu K<sub>α</sub> radiation with  $\lambda = 1.54056 \text{ \AA}$  across the  $2\theta$  range of 5° to 120° using a Malvern Panalytical Empyrean diffractometer with a step size of 0.013°  $2\theta$ . Phase analysis and refinements of the crystal structures were performed using the Rietveld algorithm<sup>49</sup> within the software HighScore Plus<sup>50</sup> using the pseudo-Voigt profile functions and a polynomial background model with four coefficients. The phase-fitting method (i.e., simultaneously with the Rietveld refinements) was used to calculate the crystallite size,  $D_i$  in the samples measured at RT, based on the differences in profile widths compared to a standard sample using the following formula:

$$D_i = \left( \frac{180}{\pi} \right) \frac{\lambda}{(W_i - W_{\text{std}})^{0.5}} \quad (1)$$

where  $W_i$  and  $W_{\text{std}}$  are the refinable profile parameters  $W$  of sample  $i$  and standard, comprised in the function that describes a variation of profile full width at half-maximum (FWHM) with Bragg angle<sup>51</sup>:

$$\text{FWHM}(\theta) = (U \tan^2 \theta + V \tan \theta + W)^{0.5} \quad (2)$$

where  $U$ ,  $V$ , and  $W$  are the profile parameters.

The variance of the crystallite size is described by:

$$\sigma^2(D_i) = \frac{A_D^2}{4(W_i - W_{\text{std}})^3} [\sigma^2(W_i) + \sigma^2(W_{\text{std}})] \quad (3)$$

with  $A_D$  representing the constant  $180 \times \lambda / \pi$ . The mean error of the crystallite size is equal to the square root of the variance.

### 2.4 | Field-emission scanning electron microscopy

The morphology of the samples was analyzed using a field-emission scanning electron microscopes from Thermo Fisher Scientific, model Axia™ ChemiSEM™ and JEOL, model JSM-7000F operating at 10 keV. Energy-dispersive

X-ray (EDX) analyzer integrated within the Thermo Fisher Scientific Axia™ ChemiSEM™ was used for elemental analysis.

The particle size distribution analysis for the samples prepared at 1200°C with a heating time 10 h was carried out using the Malvern Mastersizer 2000 laser light-scattering particle size analyzer.

### 2.5 | UV-Vis spectroscopy measurements

The UV-Vis DRS was performed on a Shimadzu UV-Vis-near-infrared (NIR) spectrometer (model UV-3600) equipped with an integrating sphere. Barium sulfate was used as a reference. The diffuse reflectance spectra were transformed using the Kubelka–Munk function and the optical bandgaps were estimated from Tauc's plots.<sup>52</sup> Emission and excitation spectra were measured in the powder samples on an Agilent Cary Eclipse fluorescence spectrometer.

### 2.6 | Photocatalytic experiments

The photocatalytic activity of NiNb<sub>2</sub>O<sub>6</sub>, CoNb<sub>2</sub>O<sub>6</sub>, and Co<sub>0.5</sub>Ni<sub>0.5</sub>Nb<sub>2</sub>O<sub>6</sub> samples characterized by PXRD and SEM was investigated by the degradation of aqueous solutions of MB under visible irradiation at 25°C. For each reaction, 3.0 mg of the powder sample was dispersed in 6.0 mL of a 5 ppm aqueous MB dye solution. Prior to irradiation, the suspension was stirred in a photoreactor (Luzchem LZC-4V) for 1 h in the dark with a magnetic stirrer to keep the mixture completely suspended (pH = 7) and to ensure the establishment of adsorption/desorption equilibrium. In the experiments with H<sub>2</sub>O<sub>2</sub> assistance, 225  $\mu\text{L}$  of 30% H<sub>2</sub>O<sub>2</sub> was added to the reaction solution (pH = 5.4) and stirred for a further 30 min to ensure adsorption/desorption equilibrium was established. Aliquots with a volume of 3 mL were then taken to measure the first point of absorbance. Then the 14 Vis lamps (Hg lamp, 8 W, 400–700 nm) were turned on to start the photodegradation in the photoreactor. After irradiation, aliquots with a volume of 3 mL were taken at regular intervals and centrifuged at 9000 rpm for 10 min. The photocatalytic degradation reactions were monitored by measuring the concentration of a degraded supernatant liquid as a function of irradiation time using a UV-Vis spectrophotometer (Varian Cary 60). The concentrations of MB were determined by measuring the absorbance at 663 nm. Before the experiments, blank tests were carried out without photocatalysts. The information extracted from the MB dye degradation curves allowed the determination of the reaction type and the calculation of the kinetic constant of the degradation reaction.

The degradation rate  $r$  of the MB dye solution can be expressed as follows<sup>53</sup>:

$$r = -d(C)/dt = k_{\text{app}}(C)^n \quad (4)$$

where  $C$  is the concentration of the MB pollutant molecules,  $k_{\text{app}}$  is the apparent-rate constant and  $n$  is the order of the reaction. The absorbance at 663 nm was used to calculate the amount of MB dye solution that was degraded over time. The percentage of degradation was calculated using the following formula<sup>53</sup>:

$$\text{Degradation (\%)} = [(C_0 - C_t)/C_0] \times 100 \quad (5)$$

where  $C_0$  and  $C_t$  are the initial concentration and the concentration after exposure to Vis light at time  $t$ , respectively. The  $k_{\text{app}}$  was calculated using the slope of the graph of  $\ln C_0/C_t$  versus the irradiation time.

To investigate the reusability of the investigated oxides, the recovered  $\text{Co}_{0.5}\text{Ni}_{0.5}\text{Nb}_2\text{O}_6$  was used after separation by centrifugation from the reaction mixture, with fresh MB solution. After each cycle, the sample was collected and washed several times with water and ethanol to remove the organic components adsorbed on the surface of the photocatalyst. It was then dried overnight at RT for the next cycle. After the reaction, the catalyst from each cycle was thoroughly rinsed several times with ethanol and dried. The recovered catalyst was reused each time for the degradation of MB dye under identical reaction conditions. The degradation activity of the catalyst was tested within four cycles and measured at the end of each cycle.

Trapping experiments were performed to identify the main reactive species involved in the degradation of MB with  $\text{Co}_{0.5}\text{Ni}_{0.5}\text{Nb}_2\text{O}_6$ . For this experiment, 1 mM of different scavengers such as benzoquinone (BQ), isopropyl alcohol (IPA) and  $\text{Na}_2\text{-EDTA}$  in aqueous dye solutions were used during the irradiation experiments to trap the superoxide radical anions, hydroxyl radicals and holes, respectively. All reaction conditions were the same as in the photocatalytic activity tests, except for the addition of the trapping agent, which was done before adding the catalysts to the solution.

## 2.7 | Impedance spectroscopy measurements

The investigation of the electrical and dielectric properties of the prepared samples was carried out using solid-state impedance spectroscopy. Polycrystalline samples were pressed into 0.2 mm thick cylindrical pellets

using a hydraulic press with a uniform load of  $2 \times 10^3$  kg. Gold electrodes, serving as contacts, with a diameter of 3.8 mm were sputtered onto both sides of the disks using the Sputter Coater SC7620 (Quorum Technologies). The complex impedance was measured using an impedance analyzer (Novocontrol Alpha-AN-Dielectric Spectrometer, Novocontrol Technologies GmbH & Co. KG) across a broad range of frequencies (0.02 Hz–0.3 MHz) at temperatures ranging from 30°C to 240°C (step 30°C) with temperature control maintained within an accuracy of  $\pm 0.2^\circ\text{C}$ . The experimental data were analyzed by electrical equivalent circuit (EEC) modeling using the complex nonlinear least-squares (CNLSQ) fitting procedure and WinFIT software.<sup>54</sup> The typical complex impedance plot manifests as one or more semicircles with the center positioned below the real axis. A resistor ( $R$ ) and a constant-phase element (CPE) were connected in parallel to form an EEC that represents an individual depressed semicircle. The CPE is an empirical impedance function of the type  $Z_{\text{CPE}} = A(j\omega)^{-\alpha}$ , where  $A$  and  $\alpha$  are the constants. The values derived from the fitting procedure, namely, resistance ( $R$ ), and electrode dimensions ( $t$  is sample thickness and  $A$  is electrode area) were used to calculate the direct current (DC) conductivity,  $\sigma_{\text{DC}} = t/(R \times A)$ .

## 3 | RESULTS AND DISCUSSION

### 3.1 | Phase analysis and microstructural characteristics of $\text{Co}_{1-x}\text{Ni}_x\text{Nb}_2\text{O}_6$ ( $x = 0, 0.5, \text{ and } 1$ )

Due to the intriguing properties and potential applications of columbite niobate-based oxides with the general formula  $\text{ANb}_2\text{O}_6$  ( $A =$  divalent alkaline-earth or transition metal cation), much work has been put into their controlled synthesis.<sup>32–42</sup> The  $\text{AO}_6$  and  $\text{NbO}_6$  octahedra, which have common edges and form separate zigzag chains along the  $c$ -axis, are formed by six oxygen atoms around the  $A$  and  $\text{Nb}$  atoms, which are arranged at  $4c$  and  $8d$  positions, respectively, in the columbite-like structure having an orthorhombic symmetry.

By optimizing the temperature range for annealing and carefully controlling the heating and cooling rates, it is possible to systematically observe the effects of the synthesis conditions on the changes in phase compositions and crystallite sizes of the final products (Figure 1 and Table 1).

Clearly, the higher the annealing temperature, the higher the orthorhombic, columbite-like  $\text{NiNb}_2\text{O}_6$  phase fraction. However, only by examining the holding times and cooling rates (see Table 1) one can reach an additional

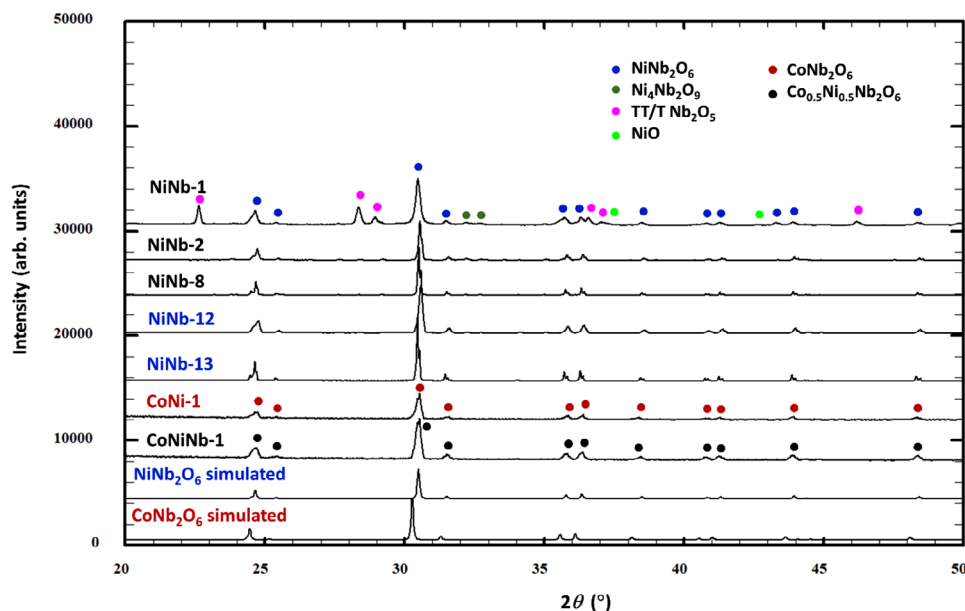


FIGURE 1 Selected cascade PXRD evolution patterns at RT of samples prepared at synthesis conditions listed in Table 1. The experimental data for orthorhombic  $\text{NiNb}_2\text{O}_6$  and  $\text{CoNb}_2\text{O}_6$  phases are corroborated by the simulated PXRD patterns (bottom) collected at ambient conditions.

level of detail and depth that leads to an understanding of the formation of the microstructurally tuned, phase-pure sample.

Heating of NiNb-1 polycrystals at  $700^\circ\text{C}$  for 24 h with a cooling rate of  $5^\circ\text{C}\cdot\text{min}^{-1}$ , resulted in the formation of 51.5 wt.% of orthorhombic  $\text{NiNb}_2\text{O}_6$  ( $a = 14.0334(6)$  Å,  $b = 5.6829(2)$  Å,  $c = 5.0243(2)$  Å,  $V = 400.69(3)$  Å<sup>3</sup>,  $R_{\text{wp}} = 11.9\%$ ) along with a significant amount of impurity phases, that is, NiO,  $\text{Ni}_4\text{Nb}_2\text{O}_9$ , and TT/ $\text{T-Nb}_2\text{O}_5$  (see Figure 1). Namely, at low temperatures, between  $500^\circ\text{C}$  and  $700^\circ\text{C}$  the TT- $\text{Nb}_2\text{O}_5$  and T- $\text{Nb}_2\text{O}_5$  show some similarities, but the crucial point is that the PXRD pattern of the TT- $\text{Nb}_2\text{O}_5$  phase contains broad peaks and a peak corresponding to a split reflection that is not present in the T- $\text{Nb}_2\text{O}_5$  phase.<sup>55–58</sup>

The structure refinement and line broadening analysis revealed that controlled annealing at  $1200^\circ\text{C}$  for 10 h and cooling within  $10^\circ\text{C}\cdot\text{min}^{-1}$  yields a phase-pure NiNb-12 sample, that is,  $\text{NiNb}_2\text{O}_6$  ( $a = 14.0328(1)$  Å,  $b = 5.68144(5)$  Å,  $c = 5.02236(4)$  Å,  $V = 400.416(6)$  Å<sup>3</sup>, s.g. *Pbcn*,  $R_{\text{wp}} = 12.8\%$ ) with a crystallite size of 87.1(1) nm (Figure 2). Heating at  $1300^\circ\text{C}$ , on the other hand, leads to the formation of a pure  $\text{NiNb}_2\text{O}_6$  phase in NiNb-13 sample, but with a nearly threefold bigger crystallite size. The isostructural oxides,  $\text{CoNb}_2\text{O}_6$  ( $a = 14.147(1)$  Å,  $b = 5.7092(4)$  Å,  $c = 5.0410(3)$  Å,  $V = 407.14(5)$  Å<sup>3</sup>, s.g. *Pbcn*,  $R_{\text{wp}} = 10.5\%$ ) and  $\text{Co}_{0.5}\text{Ni}_{0.5}\text{Nb}_2\text{O}_6$  ( $a = 14.0864(8)$  Å,  $b = 5.6942(3)$  Å,  $c = 5.0316(2)$  Å,  $V = 403.59(3)$  Å<sup>3</sup>, s.g. *Pbcn*,  $R_{\text{wp}} = 10.4\%$ ; see Figure 2) with crystallites around 50 nm in size, were synthesized using a similar method (at

$1200^\circ\text{C}$  for 10 h and cooling within  $10^\circ\text{C}\cdot\text{min}^{-1}$ ), which, to the best of our knowledge, is the first time it has been done for  $\text{Co}_{0.5}\text{Ni}_{0.5}\text{Nb}_2\text{O}_6$ . In particular, the initial structural models for NiO,  $\text{NiNb}_2\text{O}_6$ ,  $\text{Ni}_4\text{Nb}_2\text{O}_9$ , and TT- $\text{Nb}_2\text{O}_5$  phase were based on those of Rooksby et al.,<sup>59</sup> Wichmann and Mueller-Buschbaum,<sup>60</sup> Ehrenberg et al.,<sup>61</sup> and Gomes and Mohalleem,<sup>62,63</sup> respectively. Table 1 shows how temperature, holding time, and cooling rate affect the phase composition and microstructural characteristics of the columbite phase. In general, the crystallization temperature and initial cooling rate both have an effect on crystal characteristics. Crystallization with controlled cooling produces better crystal characteristics than crystallization with spontaneous cooling, as demonstrated in our work. Without a doubt, the link of cooling rates with yield, purity, and particle size distribution is of enormous importance for nanoscience, nanotechnology, and notably for the entire commercial crystallization process.<sup>64–71</sup> It is particularly crucial to manage the early phase of crystallization efficiently, since this will result in crystals of higher purity.<sup>62</sup> An increase in temperature favors the production of the columbite phase, but an increase in cooling rate reduces the crystals of the columbite phase—at  $1200^\circ\text{C}$  and a cooling rate of  $10^\circ\text{C}\cdot\text{min}^{-1}$ , the pure columbite phase has crystallites less than 100 nm in size. This defies the widely held belief that increasing temperature causes an increase in the size of crystallites in a sample. Such a phenomena is discussed in the literature in conjunction with the lowering of the surface energy of ultrafine powders—with increasing heating/cooling, the average particle size tends to drop,

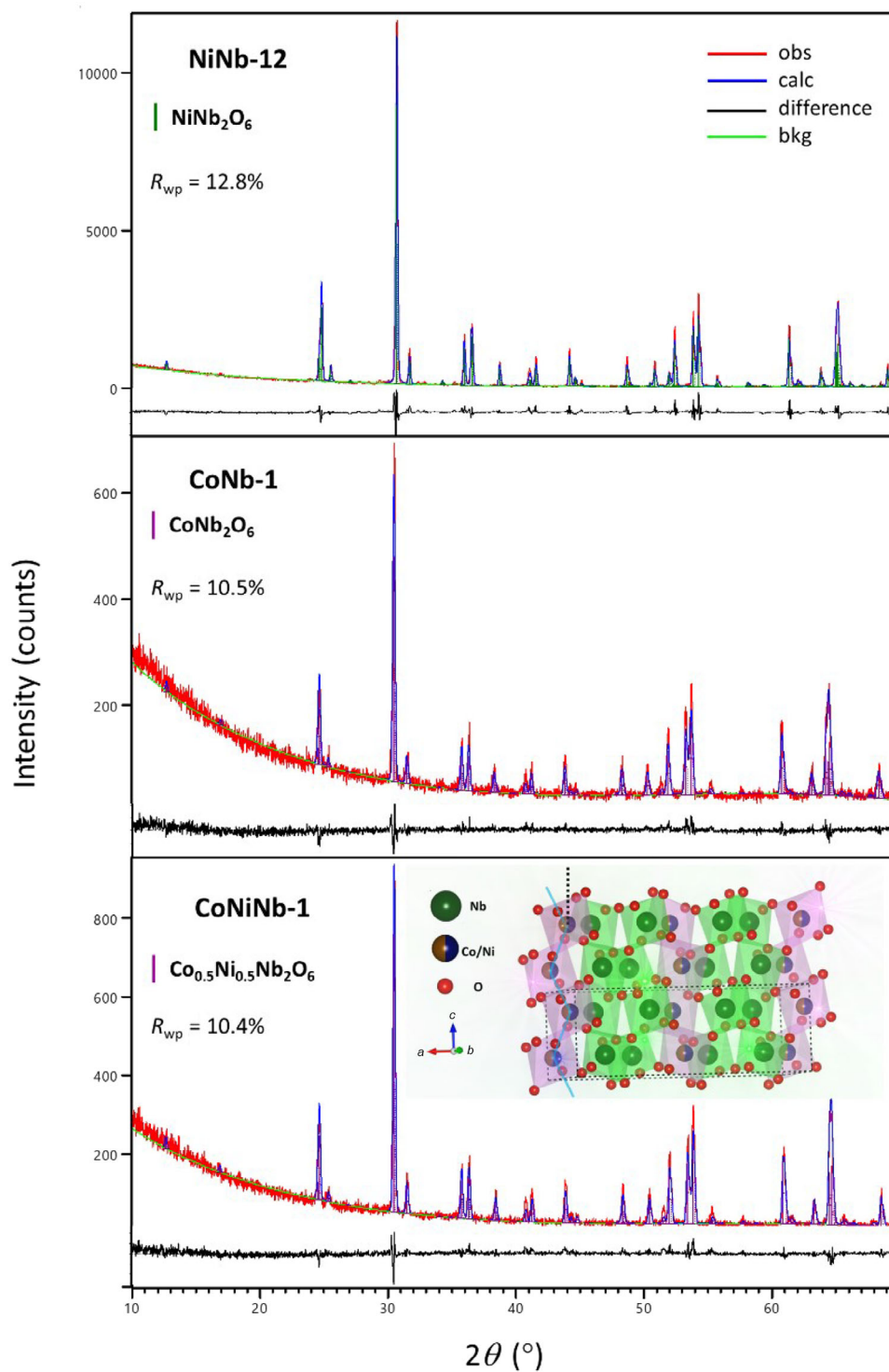


**FIGURE 2** Observed (solid red line) and calculated (solid blue line) PXR D profiles obtained from the Rietveld refinement against the PXR D data of CoNiNb-1 (bottom), CoNb-1 (middle) and NiNb-12 (top) samples at RT. The difference profiles are depicted by the lower solid black line. The green tick marks show the reflection positions of  $\text{NiNb}_2\text{O}_6$  phase, while purple tick marks depict the Bragg reflections of  $\text{NiNb}_2\text{O}_6$  and  $\text{Co}_{0.5}\text{Ni}_{0.5}\text{Nb}_2\text{O}_6$  phases. The fitted background contribution is shown by the lower solid green line. The inset (bottom) shows the spiral within the crystal structure of  $\text{Co}_{0.5}\text{Ni}_{0.5}\text{Nb}_2\text{O}_6$ . The  $\text{Co}_{0.5}\text{Ni}_{0.5}\text{Nb}_2\text{O}_6$  unit cell is depicted by dashed black lines along  $a$ -axis.

**TABLE 1** The notation of samples, synthesis conditions, and the results of quantitative phase analysis as obtained from Rietveld refinement against powder PXRD data at RT.

Sample	Annealing temperature (°C)	Holding time (h)	Heating/cooling rate (°C min <sup>-1</sup> )	Phase fraction (wt.%)	Crystallite size (nm)	R <sub>wp</sub> (%)
NiNb-1	700	24	5	NiNb <sub>2</sub> O <sub>6</sub>	52.7(1)	11.9
				Ni <sub>4</sub> Nb <sub>2</sub> O <sub>9</sub>	21.4	
				TT/T-Nb <sub>2</sub> O <sub>5</sub>	19.1	
				NiO	4.3	
NiNb-2	1000	6	5	NiNb <sub>2</sub> O <sub>6</sub>	135.4(1)	16.2
				Ni <sub>4</sub> Nb <sub>2</sub> O <sub>9</sub>	19.2	
NiNb-3	1000	18	5	NiNb <sub>2</sub> O <sub>6</sub>	172.3(1)	14.7
				Ni <sub>4</sub> Nb <sub>2</sub> O <sub>9</sub>	19.1	
NiNb-4	1100	18	5	NiNb <sub>2</sub> O <sub>6</sub>	189.3(1)	16.6
				Ni <sub>4</sub> Nb <sub>2</sub> O <sub>9</sub>	6.3	
NiNb-5	1100	24	5	NiNb <sub>2</sub> O <sub>6</sub>	193.5(1)	15.8
				Ni <sub>4</sub> Nb <sub>2</sub> O <sub>9</sub>	5.6	
NiNb-6	1100	10	10	NiNb <sub>2</sub> O <sub>6</sub>	198.9(1)	16.5
				Ni <sub>4</sub> Nb <sub>2</sub> O <sub>9</sub>	5.8	
NiNb-7	1200	3	3	NiNb <sub>2</sub> O <sub>6</sub>	144.5(1)	10.9
				Ni <sub>4</sub> Nb <sub>2</sub> O <sub>9</sub>	9.5	
				NiO	0.6	
NiNb-8	1200	3	Quenching	NiNb <sub>2</sub> O <sub>6</sub>	196.3(1)	13.3
				Ni <sub>4</sub> Nb <sub>2</sub> O <sub>9</sub>	4.5	
NiNb-9	1200	10	3	NiNb <sub>2</sub> O <sub>6</sub>	195.2(1)	11.8
				Ni <sub>4</sub> Nb <sub>2</sub> O <sub>9</sub>	4.5	
NiNb-10	1200	1	5	NiNb <sub>2</sub> O <sub>6</sub>	144.5(1)	15.5
				Ni <sub>4</sub> Nb <sub>2</sub> O <sub>9</sub>	13.9	
				NiO	1.4	
NiNb-11	1200	10	5	NiNb <sub>2</sub> O <sub>6</sub>	195.5(1)	16.2
				Ni <sub>4</sub> Nb <sub>2</sub> O <sub>9</sub>	4.9	
NiNb-12	1200	10	10	NiNb <sub>2</sub> O <sub>6</sub>	87.1(1)	12.8
NiNb-13	1300	6	5	NiNb <sub>2</sub> O <sub>6</sub>	230.2(1)	16.6
CoNb-1	1200	10	10	CoNb <sub>2</sub> O <sub>6</sub>	50.4(1)	10.5
CoNiNb-1	1200	10	10	Co <sub>0.5</sub> Ni <sub>0.5</sub> Nb <sub>2</sub> O <sub>6</sub>	52.4(1)	10.4

The standard deviations are presented within parenthesis. The crystallite sizes are calculated only for the main phase present in each sample.

but the degree of agglomeration increases<sup>71,72</sup> as can be observed from SEM micrographs.

The selected final Rietveld refinements shown in Figure 2 include parameters arising from the background function, instrumental parameters (sample displacement, scaling factor, preferred orientation), lattice parameters, and peak shape parameters, all calculated using the predicted atomic geometries. The atomic coordinates as well as temperature factors were refined exclusively for the main isostructural phases, namely, NiNb<sub>2</sub>O<sub>6</sub>, CoNb<sub>2</sub>O<sub>6</sub>, and Co<sub>0.5</sub>Ni<sub>0.5</sub>Nb<sub>2</sub>O<sub>6</sub>, all having an orthorhombic symmetry. The Rietveld refinement of CoNi-1 PXRD pattern

revealed that the initial crystal structure quite nicely fits the one of the CoNb<sub>2</sub>O<sub>6</sub> and facilitates comparison with the previously published experimental result of Weitzel,<sup>73</sup> which was also used as a starting structural model for the refinement of CoNiNb-1, that is, Co<sub>0.5</sub>Ni<sub>0.5</sub>Nb<sub>2</sub>O<sub>6</sub> phase (see Figure 2, bottom).

In particular, the equivalences for the isotropic displacement parameters  $B_{iso}$  and the  $x$ ,  $y$ , and  $z$  parameters were selected across the data sets for atoms sharing the same site symmetries (i.e., atoms Co and Ni at 4c sites). The sum of the site occupancies of Co and Ni atoms was set to unity. The  $B_{iso}$  for metal atoms were permitted to be

**TABLE 2** Summary of the resulting structural parameters and reliability factors from Rietveld refinements of NiNb-12, CoNb-1, and CoNiNb-1 against PXRD data collected at RT.

Sample	Phase	Unit cell metrics (Å) and $V$ (Å <sup>3</sup> ) s.g.			Atom	$x$	$y$	$z$	Wyck. pos.	s.o.f.	$B_{\text{iso}}$ (Å <sup>2</sup> )
		$Pbcn$	$a$	$b$							
NiNb-12	NiNb <sub>2</sub> O <sub>6</sub>	$Pbcn$	$a = 14.0328(1)$	Ni1	0	0.3446(3)	0.25	4c	1	0.93(3)	
			$b = 5.68144(5)$	Nb1	0.3415(4)	0.3194(5)	0.2516(1)	8d	1	0.46(2)	
			$c = 5.02236(4)$	O1	0.0930(3)	0.1152(2)	0.079(1)	8d	1	0.87	
			$V = 400.416(6)$	O2	0.4182(3)	0.1161(5)	0.0794(6)	8d	1	0.76	
				O3	0.2403(4)	0.1104(6)	0.4116(3)	8d	1	0.43	
CoNb-1	CoNb <sub>2</sub> O <sub>6</sub>	$Pbcn$	$a = 14.147(1)$	Co1	0	0.3180(2)	0.25	4c	1	0.43(3)	
			$b = 5.7092(4)$	Nb1	0.3381(3)	0.3240(3)	0.2520(5)	8d	1	0.86(2)	
			$c = 5.0410(3)$	O1	0.0955(5)	0.1037(6)	0.0671(4)	8d	1	0.87	
			$V = 407.14(5)$	O2	0.4242(6)	0.1151(3)	0.1121(4)	8d	1	0.76	
				O3	0.2469(8)	0.1236(4)	0.4302(5)	8d	1	0.43	
CoNiNb-1	Co <sub>0.5</sub> Ni <sub>0.5</sub> Nb <sub>2</sub> O <sub>6</sub>	$Pbcn$	$a = 14.0864(8)$	Co1	0	0.3189(5)	0.25	4c	0.5	0.46(2)	
			$b = 5.6942(3)$	Ni1	0	0.3189(5)	0.25	4c	0.5	0.46(2)	
			$c = 5.0316(2)$	Nb1	0.3388(5)	0.3246(2)	0.2523(4)	8d	1	0.89(4)	
			$V = 403.59(3)$	O1	0.0959(4)	0.1030(5)	0.0669 (7)	8d	1	0.87	
				O2	0.4246(3)	0.1157(2)	0.1126(2)	8d	1	0.76	
			O3	0.2466(9)	0.1237(6)	0.4307(6)	8d	1	0.43		

The standard deviations are presented within parenthesis.

refined without any restrictions, while the oxygen temperature factors were set at a tolerable value with negligible impact on the reliability factors. Resulting parameters and reliability factors from Rietveld refinements of NiNb-12, CoNb-1, and CoNiNb-1 are listed in Table 2.

The mixing of the molecular oxalate precursors  $[M(\text{bpy})_3]_2[\text{NbO}(\text{C}_2\text{O}_4)_3]\text{Cl}\cdot n\text{H}_2\text{O}$  (where  $M = \text{Co}^{2+}$  or/and  $\text{Ni}^{2+}$ ;  $n = 11, 12$ )<sup>48</sup> and  $(\text{NH}_4)_3[\text{NbO}(\text{C}_2\text{O}_4)_3]\cdot 3\text{H}_2\text{O}$ <sup>25</sup> under mild conditions (a mechanochemical mill is not even necessary) leads by heat treatment in one step to the desired metal composition in the oxide phases—binary and ternary columbite-like materials CoNb<sub>2</sub>O<sub>6</sub>, NiNb<sub>2</sub>O<sub>6</sub>, and Co<sub>0.5</sub>Ni<sub>0.5</sub>Nb<sub>2</sub>O<sub>6</sub> were successfully synthesized.

### 3.2 | Surface morphology

The surface morphology of the prepared oxides was examined by SEM imaging. Due to the high preparation temperature (1200°C), the NiNb<sub>2</sub>O<sub>6</sub>, CoNb<sub>2</sub>O<sub>6</sub>, and Co<sub>0.5</sub>Ni<sub>0.5</sub>Nb<sub>2</sub>O<sub>6</sub> exhibit a relatively large, densely arranged particle size of about 2–5 μm (see Figures 3 and 4). Higher magnifications SEM images reveal that particles are composed of nanometer thick stacked layers of crystals. Despite differing metal compositions, the oxides exhibit similar morphologies. The qualitative elemental composi-

tion was determined by EDX analysis (Table S1) to verify the purity of the produced materials and the distribution of certain elements in the sample. The oxides contain only the elements O, Nb, and Ni/Co or both, with no other metals detected. In addition, EDX elemental mapping was performed to understand the elemental distribution in the produced oxides. The insets in Figures 3 and 4 indicate that elements Ni, Co, Nb, and O are homogeneously distributed, demonstrating that this modified *molecular precursor-to-material* synthesis method is very effective for obtaining uniform highly crystalline ternary metal oxides.

The particle size distribution patterns of the prepared niobate oxide particles used for photocatalytic experiments are shown in Figures S1 and S2. The distribution curves show that a large fraction of the particles for all these oxides are in the range below 0.5 μm, which is slightly smaller than the particles observed with SEM imaging. This is related to the grinding and the ultrasonic conditions to which these oxides are subjected before the catalytic experiments, causing a partial splitting of the physical agglomerates observed in the SEM. According to the particle size data  $d(0.1)$ ,  $d(0.5)$ , and  $d(0.9)$  given in Table S2, the number-based average size is very similar for NiNb<sub>2</sub>O<sub>6</sub> (NiNb-12), CoNb<sub>2</sub>O<sub>6</sub> (CoNb-1), and Co<sub>0.5</sub>Ni<sub>0.5</sub>Nb<sub>2</sub>O<sub>6</sub> (CoNiNb-1). This is to be expected as all oxides were prepared by decomposition of oxalate precursor complexes using the same thermal treatment

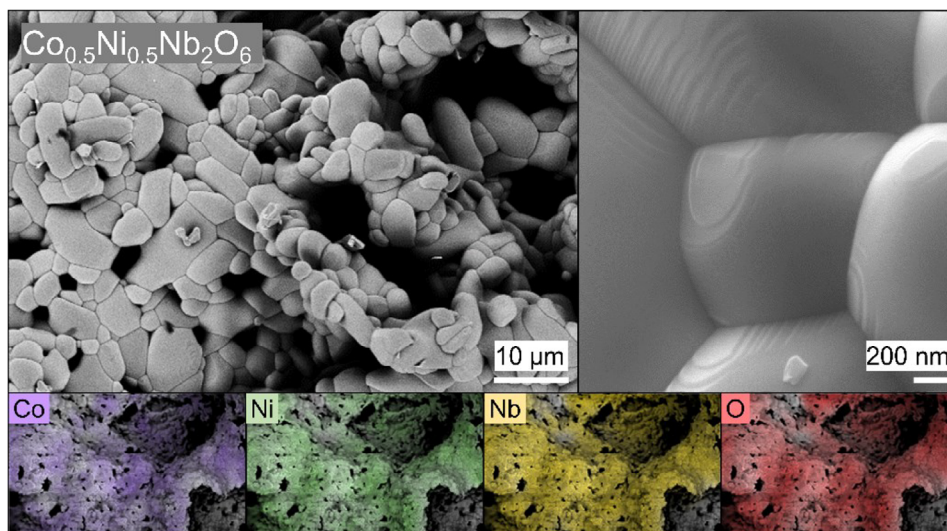


**FIGURE 3** Low and high magnification scanning electron microscopy (SEM) images of the solid solution  $\text{Co}_{0.5}\text{Ni}_{0.5}\text{Nb}_2\text{O}_6$  prepared by *molecular precursor-to-material* route at  $1200^\circ\text{C}$ . Insets show corresponding EDX element mapping with the distribution of elements Co, Ni, Nb, and O in the solid solution oxide.

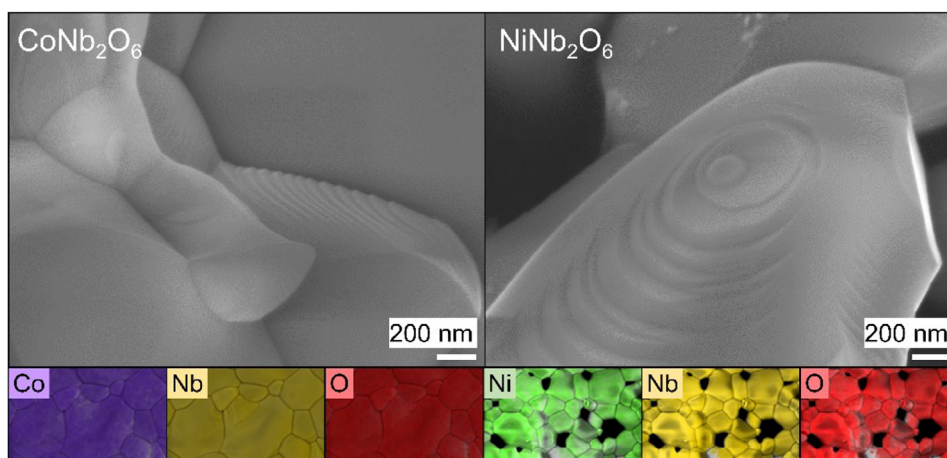


**FIGURE 4** The SEM images of the single-phase  $\text{CoNb}_2\text{O}_6$  and  $\text{NiNb}_2\text{O}_6$  prepared by *molecular precursor-to-material* route at  $1200^\circ\text{C}$ . Insets show corresponding EDX element mapping with the distribution of elements Co or Ni, Nb, and O oxides.

procedures. The volume-based average size (Table S3) shows that the  $\text{Co}_{0.5}\text{Ni}_{0.5}\text{Nb}_2\text{O}_6$  (CoNiNb-1) has only a slightly smaller average volume than  $\text{NiNb}_2\text{O}_6$  (NiNb-12) and  $\text{CoNb}_2\text{O}_6$  (CoNb-1), which together with other factors (such as crystal grain size, band gap, etc.) may reflect its better catalytic performance.

### 3.3 | Electrical characterization

Conductivity isotherms for  $\text{CoNb}_2\text{O}_6$ , chosen as representative of all studied samples, at different temperatures are shown in Figure 5A. The resulting conductivity spectra

reveal distinct features, including high-frequency dispersion and a low-frequency plateau. The high-frequency dispersion is ascribed to alternating current (AC) conductivity, whereas the low-frequency independent plateau relates to the DC conductivity of the material. The dispersive behavior is clearly visible at lower frequencies and temperatures, and as the temperature rises, it shifts to higher frequencies. Figure 5B shows conductivity isotherms at  $240^\circ\text{C}$  for each sample, illustrating differences in the DC conductivity values between them.

The DC conductivity of all samples shows a thermally activated Arrhenius-like behavior marked by a distinctive linear correlation between  $\log(\sigma_{\text{DC}}T)$  and  $1000/T$ ,

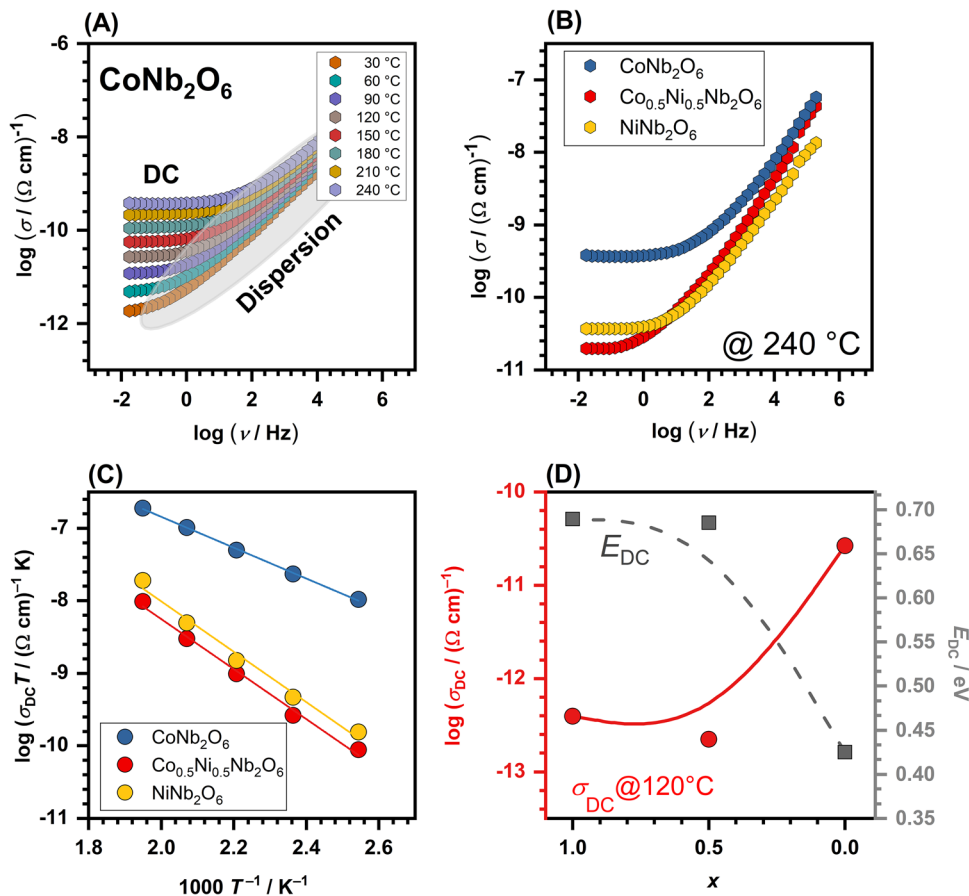


**FIGURE 5** (A) Conductivity spectra for  $\text{CoNb}_2\text{O}_6$ ; (B) Conductivity spectra for all samples measured at  $240^\circ\text{C}$ ; (C) Arrhenius plots of direct current (DC) conductivity [ $\log(\sigma_{\text{DC}}T)$  vs.  $1000/T$ ] and (D) DC conductivity at  $120^\circ\text{C}$  (full line) and activation energy for DC conductivity (dashed line) for individual samples. The lines are drawn as guides for the eye.

showcasing characteristic activation energy. In the investigated temperature range, above RT, the conduction is ascribed to the correlated barrier hopping (CBH) conduction mechanism. This process involves charge carriers leaping between sites across potential barriers that separate them, and it has been documented in columbite-like systems,<sup>74–77</sup> as well as in diverse perovskites and spinel oxides.<sup>78–80</sup> The temperature dependence of the DC conductivity is usually expressed by the following relation:

$$\sigma_{\text{DC}}T = \sigma_0^* \exp\left(\frac{-E_{\text{DC}}}{k_{\text{B}}T}\right) \quad (6)$$

where  $\sigma_{\text{DC}}$  is the DC conductivity,  $\sigma_0^*$  is the pre-exponent,  $k_{\text{B}}$  is the Boltzmann constant, and  $T$  is the temperature (K). The resulting Arrhenius equation is linearly fitted to the plot  $\log(\sigma_{\text{DC}}T)$  versus  $1000/T$ , as illustrated in Figure 5C, where the slope of the fit provides the activation energy,  $E_{\text{DC}}$ . The determined values of  $E_{\text{DC}}$  and DC conductivity given in Table 3 align well with the values reported in the literature for similar systems.<sup>74,76,77,81</sup>

Figure 5D shows the changes in the values of the DC conductivity and the activation energy that occur when  $\text{Ni}^{2+}$  is exchanged for  $\text{Co}^{2+}$ . Notably,  $\text{CoNb}_2\text{O}_6$  has the greatest  $\sigma_{\text{DC}}$  value, while  $\text{NiNb}_2\text{O}_6$  and  $\text{Co}_{0.5}\text{Ni}_{0.5}\text{Nb}_2\text{O}_6$  have similar conductivities. The observed trend in conductivity is intriguing in a number of ways. First off, processing samples at higher sintering temperatures ( $1200^\circ\text{C}$ ) may cause oxygen loss, which might result in the creation of oxygen vacancies released electrons. Since the three samples were subjected to the same heat-treatment conditions, the concentration of charge carriers, that resulted from this thermal process, should have been somewhat consistent throughout the samples, having a negligible influence on the observed trend. Second, grain size becomes an important factor to take into account. Changes in grain size can impact electrical conductivity and dielectric properties by changing the density and features of grain boundaries. In our case, owing to the high preparation temperature ( $1200^\circ\text{C}$ ), all of the samples exhibit a densely arranged particle size of about  $2\text{--}5\ \mu\text{m}$  (see Figures 3 and 4) with similar morphologies. This does not appear to have a major impact on the electrical/dielectric properties.

**TABLE 3** The values of DC conductivities,  $\sigma_{DC}$ , activation energies,  $E_{DC}$ , and selected dielectric properties of studied samples.

Sample	Phase	<sup>a</sup> $\sigma_{DC}/(\Omega^{-1} \text{ cm}^{-1})$	$E_{DC}/\text{eV}$	<sup>b</sup> $\tau_{Z''}/\text{s}$	<sup>b</sup> $\tau_{M1''}/\text{s}$	<sup>b</sup> $\tau_{M2''}/\text{s}$	<sup>c</sup> $\epsilon'(\omega)$	<sup>c</sup> $\tan\delta$
NiNb-12	NiNb <sub>2</sub> O <sub>6</sub>	$3.96 \times 10^{-13}$	0.68	$4.6 \times 10^{-2}$	$2.7 \times 10^{-2}$	$1.6 \times 10^{-3}$	5.7	0.008
CoNb-1	CoNb <sub>2</sub> O <sub>6</sub>	$2.64 \times 10^{-11}$	0.42	$9 \times 10^{-3}$	$6 \times 10^{-3}$	$1.9 \times 10^{-4}$	9.1	0.033
CoNiNb-1	Co <sub>0.5</sub> Ni <sub>0.5</sub> Nb <sub>2</sub> O <sub>6</sub>	$2.24 \times 10^{-13}$	0.69	$2.3 \times 10^{-1}$	$1.2 \times 10^{-1}$	$1.8 \times 10^{-3}$	11.1	0.007

<sup>a</sup>at 120°C;<sup>b</sup>at 240°C;<sup>c</sup>at 10 kHz.

Therefore, the key element affecting the DC conductivity trend in the current research is linked to the unique electronic configuration of the different transition metal ions (Co<sup>2+</sup> and Ni<sup>2+</sup>) and their consequential impact on the conduction mechanism.<sup>75,77,82</sup> The Co<sub>0.5</sub>Ni<sub>0.5</sub>Nb<sub>2</sub>O<sub>6</sub> exhibits a distinctive behavior, where the combination of Co<sup>2+</sup> and Ni<sup>2+</sup> ions in a 1:1 ratio introduces a complex interplay of their respective effects on the conductivity. The interactions between mixed metal centers disrupt the lattice, confining active electrons and resulting in a decrease in conductivity.<sup>83</sup> Surprisingly, the DC conductivity for this sample does not display a monotonic shift with composition modifications, nor does it lie between the values seen for samples containing solely Co<sup>2+</sup> or Ni<sup>2+</sup>. In contrast, the DC conductivity for the mixed sample shows a minimum value, followed by a maximum in energy activation (see Figure 5D and Table 3). In contrast to the CoNb<sub>2</sub>O<sub>6</sub> sample, which has the highest DC conductivity and lowest energy activation of 0.42 eV, the observed value is similar to the NiNb<sub>2</sub>O<sub>6</sub> sample, but both samples exhibit two orders of magnitude lower DC. This can be attributed to the higher numbers of unpaired electrons for Co<sup>2+</sup> in the outer electron shell. The sample Co<sub>0.5</sub>Ni<sub>0.5</sub>Nb<sub>2</sub>O<sub>6</sub> exhibits minimal conductivity, indicating that structural features hinder electrical transport in this mixed system, even with an increase in charge carriers. This highlights the intricate relationship in the system under study between the material composition, structural features, and electrical properties.

For sample Co<sub>0.5</sub>Ni<sub>0.5</sub>Nb<sub>2</sub>O<sub>6</sub>, the imaginary component of the modulus revealed a temperature-dependent peak,  $M''_{\text{max}}$ , indicating the electrical relaxation nature (Figure 6A). The asymmetry of the peak suggests a nonuniform relaxation process and possible contributions from more than one relaxation process whose maxima overlap due to similar relaxation times. The frequency domain preceding the peak maximum  $M''$  defines the regime where charge carriers exhibit long-range mobility. In contrast, as frequencies surpass the peak maximum, carriers experience confinement within potential wells, restricting their mobility to shorter distances. Peaks in the  $M''$  curves, in particular, display an asymmetric and broader profile, deviating from the idealized Debye curve. Similar behavior

is observed in other samples investigated in this study. Like  $M''$ ,  $Z''$  exhibits a temperature-dependent peak at a particular frequency. A single maximum in the lower frequency region indicates that the process at a lower frequency, characterized by higher resistance, overshadows the process at a higher frequency. Furthermore, the normalized plot  $Z''/Z''_{\text{max}}$  versus  $f/f_{Z''_{\text{max}}}$  (inset in Figure 6B) provides the FWHM of  $\approx 1.9$  decades, surpassing the 1.14 decades for Debye-type FWHM. This discrepancy indicates a deviation from ideal Debye-type relaxations, suggesting a non-Debye type of relaxation.<sup>74,76,84</sup> Moreover, the  $M''$  curve exhibits an even greater FWHM value ( $\approx 3.3$  decades). For CoNb<sub>2</sub>O<sub>6</sub> and NiNb<sub>2</sub>O<sub>6</sub>, these values are slightly lower, being 1.8 ( $Z''$ ) and 2.9 ( $M''$ ) for CoNb<sub>2</sub>O<sub>6</sub>, and 1.6 ( $Z''$ ) and 2.7 ( $M''$ ) for NiNb<sub>2</sub>O<sub>6</sub>, respectively. Figure 6C depicts normalized  $M''$  and  $Z''$  curves for the Co<sub>0.5</sub>Ni<sub>0.5</sub>Nb<sub>2</sub>O<sub>6</sub> sample, serving as representatives of all the samples in this study. The superimposed nature of  $M''/M''_{\text{max}}$  and  $Z''/Z''_{\text{max}}$  curves reveals two distinct relaxation processes. The  $Z''$  curve displays a single maximum that nearly aligns with the first of the two maxima in the  $M''$  curve, marked  $f_{M1''}$ , it is assigned to the same relaxation process, that is, grain boundary. The second peak, marked  $f_{M2''}$ , is related to grain contribution.

By identifying the frequency corresponding to the peak maximum in  $M''$  and  $Z''$  curves, the relaxation times,  $\tau_{Z''}$  and  $\tau_{M''}$ , at a specific temperature can be calculated using the equation  $\tau = 1/(2\pi\nu)$ . The calculated relaxation times, as shown in Table 3, follow the opposite trend compared to the DC conductivity trend, with the fastest relaxation times observed for the sample with the greatest DC conductivity value, supporting the relationship between electrical properties and relaxation times. To elucidate the distinct contributions to overall conductivity, the results of impedance measurements are presented in the complex impedance plane through the Nyquist plots, as depicted in Figure 6D. The shape of each complex impedance spectrum is directly influenced by various processes and effects, including the existence of grain boundaries. In this study, we applied an EEC modeling approach to Nyquist plots using the CNLLSQ fitting procedure.

At first glance, only a single semicircle is apparent in the complex impedance plots, owing to high resistance

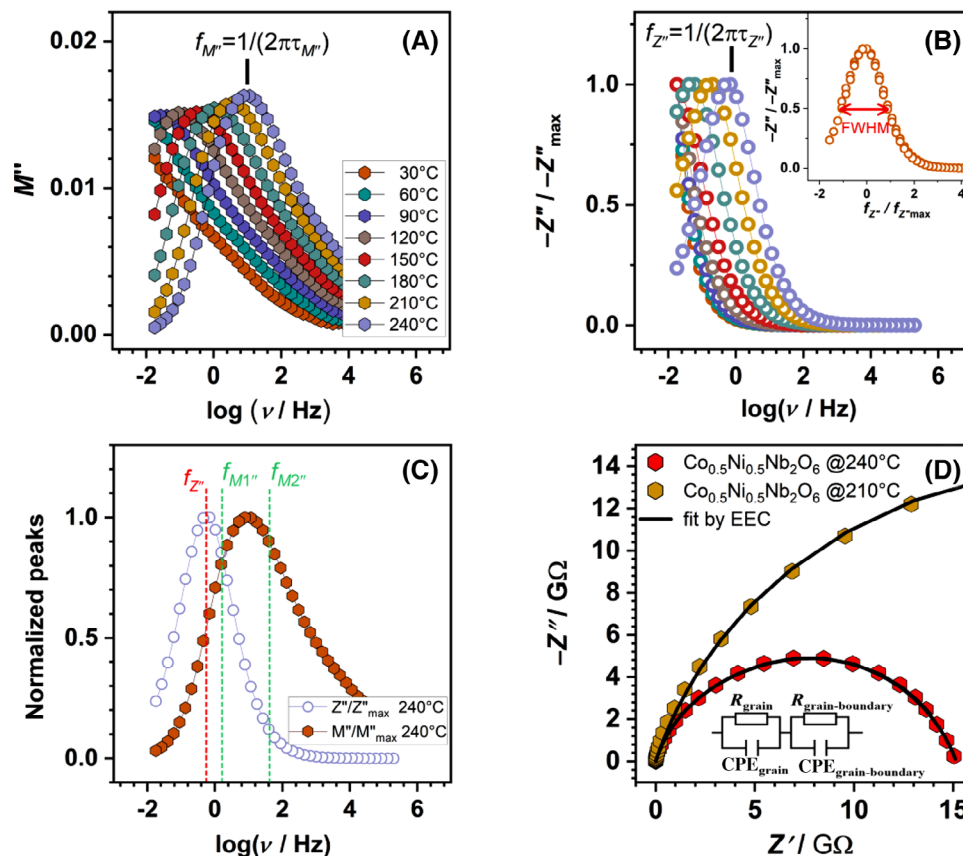


**FIGURE 6** (A) The frequency variation of imaginary part  $M''$  of complex modulus spectra at different measured temperatures for sample  $\text{Co}_{0.5}\text{Ni}_{0.5}\text{Nb}_2\text{O}_6$ ; (B) The plot of  $Z''/Z''_{\max}$  versus frequency, where inset is the normalized plot  $Z''/Z''_{\max}$  versus  $f_{Z''}/f_{Z''\max}$ ; (C) Frequency dependence of normalized  $M''$  and  $Z''$  curves, and (D) Complex impedance plot at 210 and 240°C for sample  $\text{Co}_{0.5}\text{Ni}_{0.5}\text{Nb}_2\text{O}_6$  with corresponding equivalent circuit used for fitting the data is shown in the inset.

and the predominance of one specific process or effect, see Figure 6D. However, based on the previous analysis of frequency maxima derived from the imaginary components of the modulus and impedance (see Figure 6A–C), it was deduced that the second process exists at higher frequencies, though barely visible due to lower resolution. Subsequently, the experimental data are fitted onto two  $R$ -CPE circuits connected in series. The high-frequency semicircle is ascribed to grain contribution, whereas the predominant low-frequency semicircle represents the response from grain boundaries. The obtained capacitance values for both relaxation processes fall within the range of  $10^{-11}$  F and are associated with significant grain fractions and grain boundaries.<sup>85,86</sup> On the other hand, the resistance values of the grain boundary consistently exceed the grain resistance values (by a factor of 10) across all samples, and the corresponding semicircles are more depressed, which is consistent with the results of relaxation studies, emphasizing their dominant role in electrical contributions in these columbite systems. The Nyquist plots reveal a reduction in the size of the semicircles as the measurement temperature rises, as illustrated by the dark-yellow data points at

210°C and the red data points at 240°C (see Figure 6D). This suggests that the resistance introduced by both the grain and grain boundary to charge transport diminishes with increasing measurement temperatures.

The real component of complex permittivity,  $\epsilon'(\omega)$ , also known as the dielectric permittivity, is depicted in Figure 7A, showcasing its frequency-dependent behavior at various temperatures for  $\text{CoNb}_2\text{O}_6$ , which serves as a representative sample. The  $\epsilon'$  spectra exhibit two characteristic regions: dispersion, which occurs at lower frequencies, and a constant value,  $\epsilon_{\infty}$ , achieved at higher frequencies. This constant value of  $\epsilon_{\infty}$  results from the fast polarization processes occurring in the samples under the applied field.

Figure 7A further shows that as the temperature rises, the frequency range dominated by charge carrier contribution expands, as charges acquire sufficient energy to overcome barriers and be released.<sup>74,75</sup> To further elucidate the impact of frequency and temperature on dielectric permittivity, the values of  $\epsilon'$  at the three selected frequencies across the measured temperature range are illustrated in Figure 7B. It can be seen that as the frequency rises,

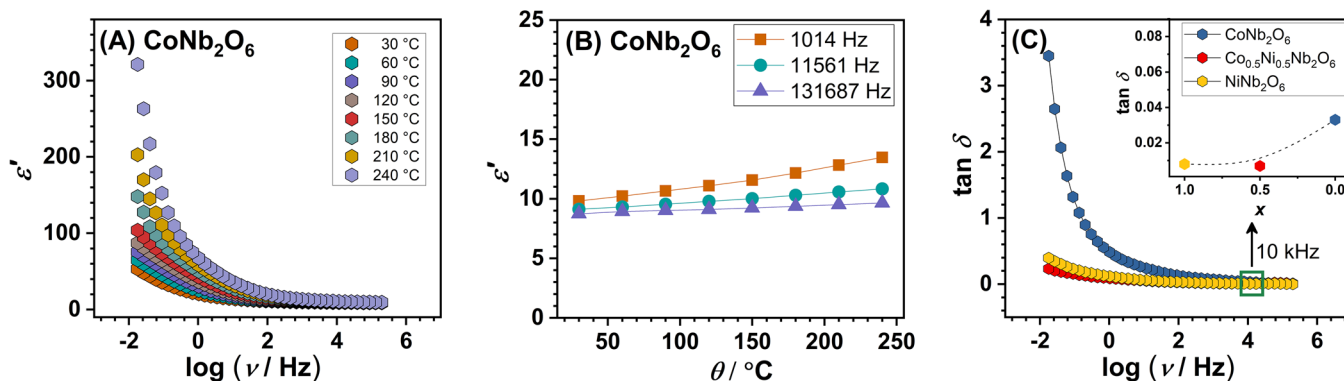


FIGURE 7 (A) Frequency and temperature dependence of dielectric permittivity for  $\text{CoNb}_2\text{O}_6$ ; (B) Temperature dependence of dielectric permittivity for  $\text{CoNb}_2\text{O}_6$ , at various frequencies and (C) Frequency dependence of loss factor,  $\tan\delta$ , for all samples at  $30^\circ\text{C}$ . The inset in (C) shows the compositional dependence of  $\tan\delta$  for all samples at  $30^\circ\text{C}$  and 10 kHz.

$\epsilon'$  values become almost temperature-independent. Interestingly, the literature sources reported different dielectric permittivity values for  $\text{CoNb}_2\text{O}_6$  (20.5,<sup>87</sup> 22.0,<sup>88</sup> 22.8<sup>77</sup>) and  $\text{NiNb}_2\text{O}_6$  (22.6<sup>77</sup>), which are greater than the experimental values found in this study, as shown in Table 3. The difference between the experimental values of  $\epsilon'$  in this study and the literature data can be attributed to the fact that permittivity data are directly influenced by sample thickness.<sup>89,90</sup> The samples in this study were very thin ( $\sim 0.2$  mm).

All samples had a low dielectric loss (Figure 7C), with  $\text{NiNb}_2\text{O}_6$  and  $\text{Co}_{0.5}\text{Ni}_{0.5}\text{Nb}_2\text{O}_6$  having almost identical values. It is worth noting that the composition dependence of  $\tan\delta$  closely aligns with the trend observed in DC conductivity (see Figure 5D). The  $\text{CoNb}_2\text{O}_6$  has the greatest value due to its higher conductivity,<sup>91</sup> whereas  $\text{Co}_{0.5}\text{Ni}_{0.5}\text{Nb}_2\text{O}_6$  has the lowest  $\tan\delta$  value. These results indicate a remarkable influence of the cations present in these systems on both  $\epsilon'$  and  $\tan\delta$  values, consistent with previous research.<sup>77</sup>

Although the electrical/dielectric experiments in this study were conducted in atmosphere of pure nitrogen (no illuminated conditions), they provide valuable insights into the intrinsic charge transfer dynamics of the material. By examining the conductivity, dielectric properties and relaxation processes using impedance spectroscopy, we gain a clearer understanding of how charge carriers behave within the material under the influence of structural features. Observations such as the CBH mechanism and the role of grain boundaries in charge transport are important to understand how the material might function in a photocatalytic setting, where efficient charge separation and transport are critical. While this study does not cover electrochemical studies under light exposure, future work in this area that we plan, could provide significant insights for a more comprehensive understand-

ing. In particular, how the electrical/dielectric properties of the material in illuminated environments, impact its performance in applications such as photocatalysis and solar-driven energy conversion. We plan to continue these investigations in future research to fully explore the potential of  $\text{Co}_{1-x}\text{Ni}_x\text{Nb}_2\text{O}_6$  under realistic operating conditions.

As mentioned above, the  $\text{NiNb}_2\text{O}_6$  has already shown promise as an anode material in lithium-ion batteries as it exhibits high performance and stability, making this family of oxides very suitable for next-generation energy storage devices.<sup>38,39</sup> The high dielectric permittivity and low dielectric loss of these materials, particularly of  $\text{Co}_{0.5}\text{Ni}_{0.5}\text{Nb}_2\text{O}_6$ , suggest that they could be useful as dielectric materials in resonators and capacitors.<sup>35</sup> The dependence of conductivity on temperature and frequency, together with the non-Debye-type relaxation processes, opens up potential applications in temperature and possibly humidity sensors. These materials could be used for the development of sensitive devices that detect changes in environmental conditions, as their electrical properties can be tuned and adapted to specific sensing applications. We therefore plan to continue this study in this direction.

### 3.4 | UV-Vis spectroscopy measurements and photocatalytic degradation of MB dye

The experimental optical DRS spectra of  $\text{CoNb}_2\text{O}_6$ ,  $\text{NiNb}_2\text{O}_6$ , and  $\text{Co}_{0.5}\text{Ni}_{0.5}\text{Nb}_2\text{O}_6$  were measured in the range of 300–1200 nm. As shown in Figure 8 all oxides exhibit absorption bands in the visible part of the spectrum. The bands at 446 and 824 nm in the spectrum of  $\text{NiNb}_2\text{O}_6$  oxide are related to spin-allowed transitions in  $\text{NiO}_6$  octahedron:  ${}^3T_{1g}(P) \leftarrow {}^3A_{2g}$  and  ${}^3T_{1g} \leftarrow {}^3A_{2g}$ , respectively. Two spin-forbidden transitions, to  ${}^1T_{1g}$  and  ${}^1E_g$

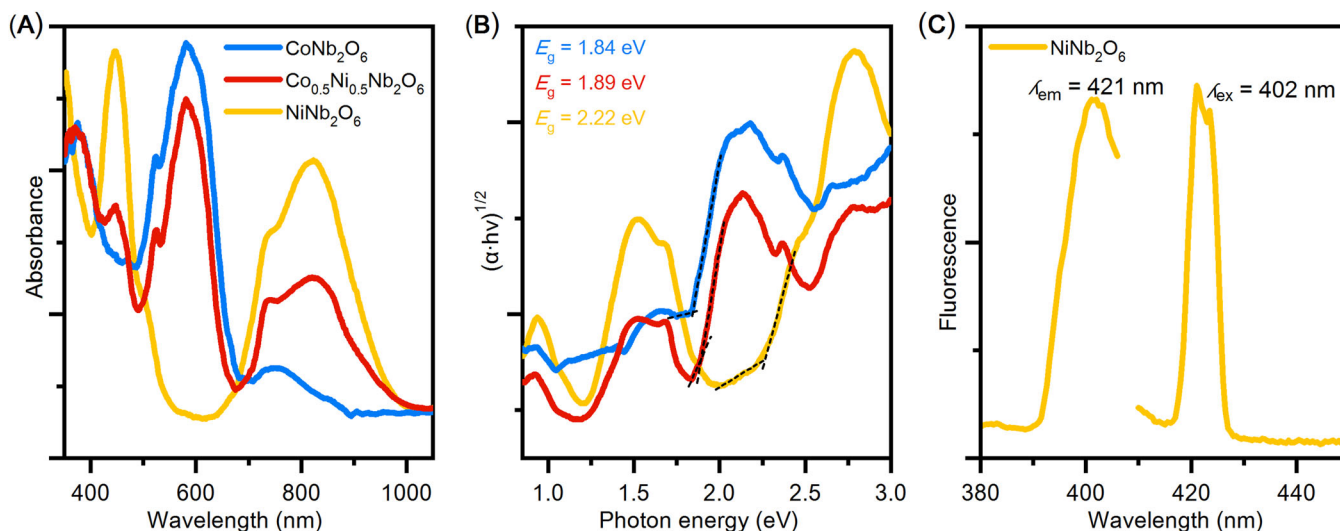


**FIGURE 8** The optical properties of  $\text{CoNb}_2\text{O}_6$ ,  $\text{NiNb}_2\text{O}_6$ , and  $\text{Co}_{0.5}\text{Ni}_{0.5}\text{Nb}_2\text{O}_6$ : (A) Kubelka–Munk diffuse reflectance absorption spectra ranging from 350 to 1050 nm; (B) Tauc's plots corresponding to indirect transitions; (C) Excitation ( $\lambda_{\text{em}} = 421 \text{ nm}$ ) and emission ( $\lambda_{\text{ex}} = 402 \text{ nm}$ ) spectra of the  $\text{NiNb}_2\text{O}_6$  samples prepared at  $1200^\circ\text{C}$ .

levels, are also observed as bands around 500 and 740 nm. These bands are also present in the  $\text{Co}_{0.5}\text{Ni}_{0.5}\text{Nb}_2\text{O}_6$ , along with bands typical of cobalt(II) in octahedral environment, namely, the spin allowed transitions  ${}^4T_{1g}(P) \leftarrow {}^4T_{1g}$  and  ${}^4A_{2g} \leftarrow {}^4T_{1g}$ , appearing as bands at  $\sim 524$  and  $582 \text{ nm}$ , respectively. The spectrum of  $\text{CoNb}_2\text{O}_6$  shows only bands related to cobalt(II) in octahedral environment.<sup>92</sup>

Tauc's plots from diffuse reflectance measurements were calculated to estimate the band gap energy of prepared oxides. The DFT calculations revealed that  $\text{NiNb}_2\text{O}_6$  and  $\text{CoNb}_2\text{O}_6$  had an indirect band gap allowed at photon energies of 2.8 and 1.8 eV, respectively.<sup>93,94</sup> The results presented here are in fair agreement with calculated values and earlier experimental studies,<sup>95,96</sup> indicating a band gap of 1.84 eV for  $\text{CoNb}_2\text{O}_6$ , 2.22 eV for  $\text{NiNb}_2\text{O}_6$  and 1.89 eV for  $\text{Co}_{0.5}\text{Ni}_{0.5}\text{Nb}_2\text{O}_6$ . For  $\text{NiNb}_2\text{O}_6$  oxide fluorescence measurements at RT (Figure 8C) reveal a blue emission centered at 421 nm upon 402 nm excitation, which is consistent with earlier literature reports on the photoluminescence properties of  $\text{NiNb}_2\text{O}_6$ .<sup>41,96</sup>

The main source of textile wastewater pollution are dyes, which are not biodegradable due to their extreme chemical stability. They have harmful effects on both the aquatic life and human health. Additionally, they affect the color of the water and reduce the light transmission of the water. Therefore, the most important thing is to find a simple and efficient way for treating the wastewater. The photocatalytic process is a very efficient, cost-effective, and environmentally friendly treatment compared to existing technologies. Hence, many binary and ternary oxide semiconductors have been investigated with regard to dye degradation.<sup>97–99</sup> In contrast, photocatalytic materials that

can utilize visible light are more attractive than those that function under UV light, which accounts for less than 5% of the total energy emitted by the sunlight. The photocatalysts in the visible light area ( $420 \text{ nm} < \lambda < 800 \text{ nm}$ ) may be formed by oxides with a band gap of 2 eV, as shown by previous research.<sup>100–102</sup>

The photocatalytic properties of columbite  $\text{Co}_{1-x}\text{Ni}_x\text{Nb}_2\text{O}_6$  ( $x = 0, 0.5, \text{ and } 1$ ) were investigated by studying the degradation of aqueous solutions of MB dye under visible light. Despite suitable band gap energies the irradiation process revealed a rather poor photocatalytic efficiency of the studied oxide materials in the degradation of organic dye (see Figures S3 and S4). The absorption peak of the MB dye in the spectra remains constant as the irradiation period increases.

For the samples annealed at higher temperatures the average particle size of an oxide inevitably grows. In general, an increase in the average particle size reduces the specific surface area, which in turn reduces the density of active sites on the surface and also increases the recombination rate of electrons and holes on the surface of the catalysts. Both factors have a negative effect on photocatalytic degradation, which could explain partly poor photocatalytic performance of the studied oxides. On the other hand, the energy band gap decreases with increasing particle size. The reduction in the band gap leads to optical absorption in the visible part of the spectrum, which enhances photocatalytic degradation under sunlight.<sup>103</sup>

The literature on the photocatalytic properties of columbite  $\text{Co}_{1-x}\text{Ni}_x\text{Nb}_2\text{O}_6$  ( $x = 0, 0.5, \text{ and } 1$ ) is very scarce and refers mainly to the  $\text{NiNb}_2\text{O}_6$ . It was found

that  $\text{NiNb}_2\text{O}_6$  with different varying amounts of graphene oxide (RGO; 5, 10, and 15 wt.%) prepared hydrothermally by ultrasonic synthesis were exposed to visible light for the degradation of doxycycline (DOX) and tetracycline hydrochloride (TC) in water. The binary nanocomposites increased activity compared to  $\text{NiNb}_2\text{O}_6$  (64.3% and 59.8%), with the highest activity achieved for the 10 wt.% RGO sample ( $\text{NiNb}_2\text{O}_6/10$  wt.% RGO) which degraded 89.2% and 94.1% DOX and TC, respectively, in 80 min.<sup>96</sup> The potential of  $\text{NiNb}_2\text{O}_6$  as a water splitting photocatalyst was also investigated. It was found that  $\text{H}_2$  evolution from water with pure  $\text{NiNb}_2\text{O}_6$  under visible light had a very low rate, although this could be improved by surface modification to suppress electron–hole recombination.<sup>42</sup> Recently, the construction of three-dimensional (3D)/two-dimensional (2D) heterojunctions has been considered as a viable strategy to overcome the fast recombination of charge carriers. To this end, a 3D  $\text{NiNb}_2\text{O}_6$ –2D E-g $\text{C}_3\text{N}_4$  (graphitic carbon nitride) type-II heterojunction was prepared as a dual catalyst for photoreduction of  $\text{Cr}^{6+}$  to  $\text{Cr}^{3+}$  and the photo-oxidation of MB, malachite green (MG), and crystal violet (CV) under visible light. The band gap and photocatalytic activity were also investigated for pure  $\text{NiNb}_2\text{O}_6$ . Among the prepared catalysts, the NG-20 composite (80% of  $\text{NiNb}_2\text{O}_6$  and 20% of E-g $\text{C}_3\text{N}_4$ ) exhibits excellent photocatalytic activity in removing 97% of  $\text{Cr}^{6+}$  in 120 min and degrading 97.4%, 96.1%, and 98% of MB, MG, and CV, respectively in 20 min under direct sunlight.<sup>104</sup>

In order to improve the photocatalytic activity of Co, Ni niobate oxides by generating more highly reactive hydroxyl radicals and avoiding the hole–electron recombination,  $\text{H}_2\text{O}_2$ -assisted degradation was used.<sup>105–107</sup> In general,  $\text{H}_2\text{O}_2$  accepts electrons from the conduction band and immediately converts to  $\text{OH}^\bullet$  radicals, which favors the concentration of holes for the oxidation process. It is known that the generated holes are mainly involved in the recombination process, but not in the formation of the  $\text{OH}^\bullet$  radicals, since the reaction time for the formation of the  $\text{OH}^\bullet$  radicals ( $\sim 10^{-3}$  s) is much longer than the recombination time at the surface ( $\sim 10^{-12}$  s). These strongly oxidizing radicals react with the organic dyes, and lead to a destructive oxidation process in the dyes.<sup>106</sup> In addition, the  $\text{H}_2\text{O}_2$  is a better electron acceptor than  $\text{O}_2$ .<sup>107</sup>

The optical absorption spectra of the MB dye solutions with the electron-capturing agent  $\text{H}_2\text{O}_2$  after different irradiation time intervals in the presence of  $\text{CoNb}_2\text{O}_6$ ,  $\text{NiNb}_2\text{O}_6$ , and  $\text{Co}_{0.5}\text{Ni}_{0.5}\text{Nb}_2\text{O}_6$  are shown in Figure 9. The absorption peaks of MB dye gradually decrease with increasing irradiation time, suggesting a decrease in dye concentration in the solution due to the degradation. The degrading impact of  $\text{H}_2\text{O}_2$  on MB was evaluated without catalysts. Figure 9 shows the optical absorption spectra of the MB dye in the presence of the assisting agent  $\text{H}_2\text{O}_2$

at different irradiation time intervals. After 270 and 330 min of irradiation, the MB pollutant degraded by 48% and 52%, respectively. The characteristic absorption peak of the MB model pollutant in the presence of  $\text{H}_2\text{O}_2$  and the photocatalysts  $\text{CoNb}_2\text{O}_6$ , and  $\text{NiNb}_2\text{O}_6$  was degraded by 78% and 87%, respectively, after 330 min of irradiation (Figure 9). In the presence of  $\text{H}_2\text{O}_2$  and the photocatalyst  $\text{Co}_{0.5}\text{Ni}_{0.5}\text{Nb}_2\text{O}_6$  the characteristic absorption peak of the MB dye was reduced for 90% within a time interval of 270 min. The degradation efficiency of MB dye pollutant in the presence of  $\text{H}_2\text{O}_2$  was calculated based on the curves of  $C/C_0$  versus irradiation time, as shown in Figure 10A. It is evident that the degradation efficiency of MB in the presence of  $\text{H}_2\text{O}_2$  and the photocatalysts was about 26% for  $\text{CoNb}_2\text{O}_6$ , 35% for  $\text{NiNb}_2\text{O}_6$ , and 38% for  $\text{Co}_{0.5}\text{Ni}_{0.5}\text{Nb}_2\text{O}_6$ , which exhibit the best photocatalytic activity in the series.

In order to understand the reaction kinetics of dye degradation, curves of  $\ln(C/C_0)$  versus time were generated for all three samples. The plot of the reaction kinetics points to the Langmuir–Hinshelwood model, indicating that the reaction is pseudo-first-order (Figure 10B). The concentration of MB decreases gradually, and it is evident that the reduction follows an essentially linear trend (Table S4). The  $k_{\text{app}}$  values of the products increased from  $4.09 \times 10^{-3} \text{ min}^{-1}$  to  $7.81 \times 10^{-3} \text{ min}^{-1}$ , in the order  $\text{Co}_{0.5}\text{Ni}_{0.5}\text{Nb}_2\text{O}_6 > \text{NiNb}_2\text{O}_6 > \text{CoNb}_2\text{O}_6$ , whereas  $k_{\text{app}}$  was  $2.12 \times 10^{-3} \text{ min}^{-1}$  in the blank experiment (Figure 10A and Table S4).

These experiments show that the presence of  $\text{H}_2\text{O}_2$  plays a crucial role in the photocatalytic mineralization of MB under Vis irradiation, especially for the photocatalyst  $\text{Co}_{0.5}\text{Ni}_{0.5}\text{Nb}_2\text{O}_6$ . Remarkably, it turned out that the electron capturing agent was important to control the surface recombination process in the investigated oxides, enhancing the photocatalytic degradation activity. Since the photocatalytic activity of the prepared and tested oxides  $\text{Co}_{1-x}\text{Ni}_x\text{Nb}_2\text{O}_6$  ( $x = 0, 0.5, \text{ and } 1$ ) in the decomposition of MB dyes under Vis irradiation has not been investigated so far, it is not possible to compare the maximum degradation efficiency obtained for the same oxides prepared by a different method.

To investigate the reusability and stability of the investigated oxides as photocatalysts, repeated degradation experiments were performed under the same photocatalytic conditions, with the oxide showing the highest degradation efficiency. Figure 11 shows the reusability of four runs in the presence of  $\text{Co}_{0.5}\text{Ni}_{0.5}\text{Nb}_2\text{O}_6$  as a photocatalyst for MB degradation. After the catalyst was reused four times, it maintained its photocatalytic behavior, but the MB degradation efficiency was slightly lower after two cycles. In addition, the structural stability of the sample used as photocatalyst for the degradation of MB in four cycles was demonstrated by PXRD patterns.

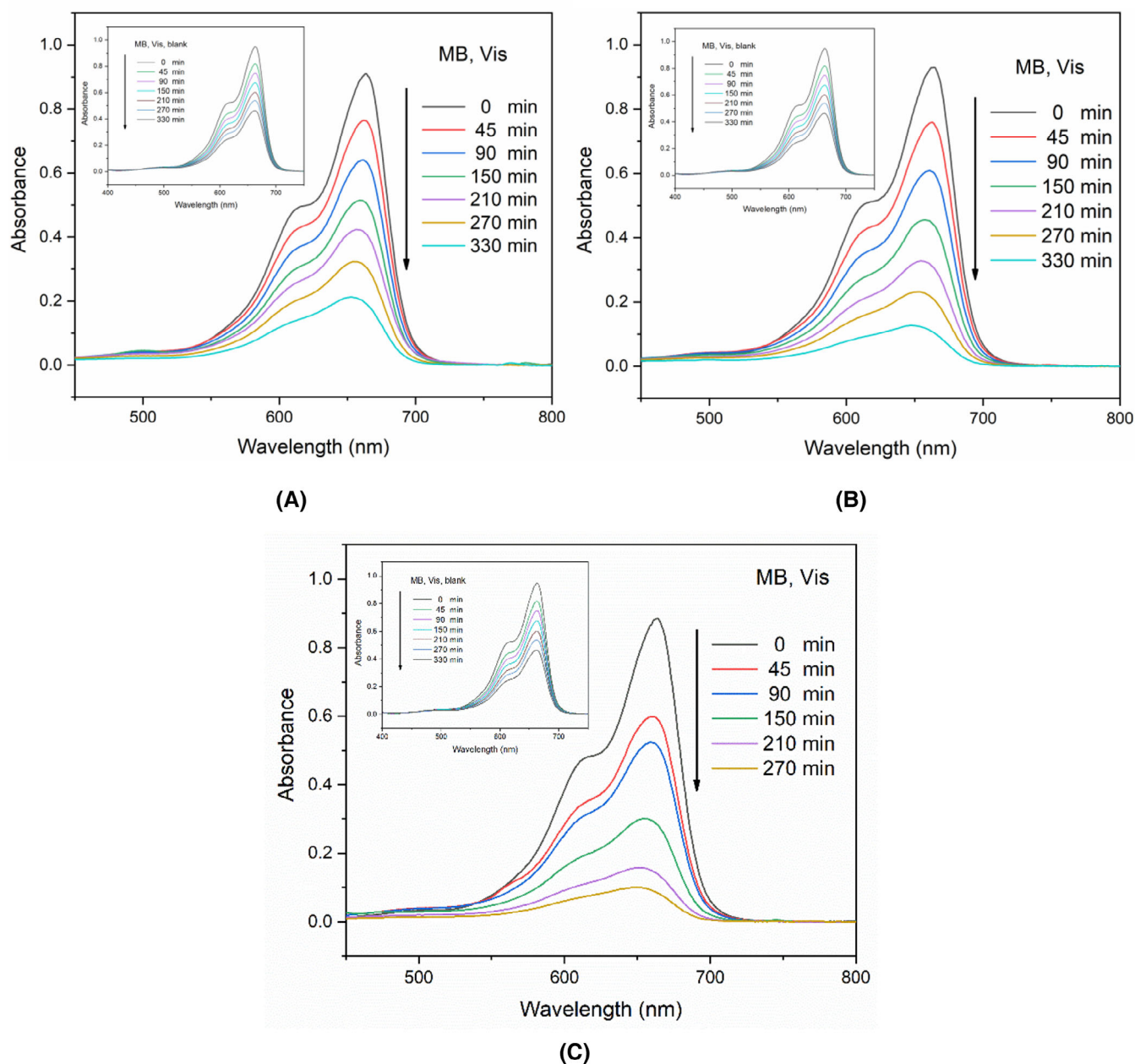


**FIGURE 9** Time-dependent UV-Vis absorption spectra of the decomposition of MB dye solutions under visible irradiation in the presence of  $\text{H}_2\text{O}_2$  and (A)  $\text{CoNb}_2\text{O}_6$ , (B)  $\text{NiNb}_2\text{O}_6$ , and (C)  $\text{Co}_{0.5}\text{Ni}_{0.5}\text{Nb}_2\text{O}_6$ . The corresponding blank experiments are shown in insets.

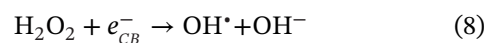
No structural changes of the sample occurred during the degradation of the organic dye, which can be clearly seen in Figure S5, indicating its stability. The results show that the synthesized materials are suitable for practical application due to their reusability and structural stability.

Under Vis irradiation, the valence band electrons of the composite photocatalyst are excited into the conduction band, leaving the holes in the valence band. Of the resulting electron-hole pairs, some are involved in recombination and the rest move on the surface to partic-

ipate in the chemical reaction with the electron acceptor and donor.<sup>105–107</sup> The photogenerated electrons react with dissolved  $\text{O}_2$  to form superoxide radical anions ( $\text{O}_2^{\cdot-}$ ):



In addition,  $\text{H}_2\text{O}_2$  accepts electrons from the conduction band and immediately converts to  $\text{OH}^{\cdot}$  radicals, which favors the concentration of holes for the oxidation process:



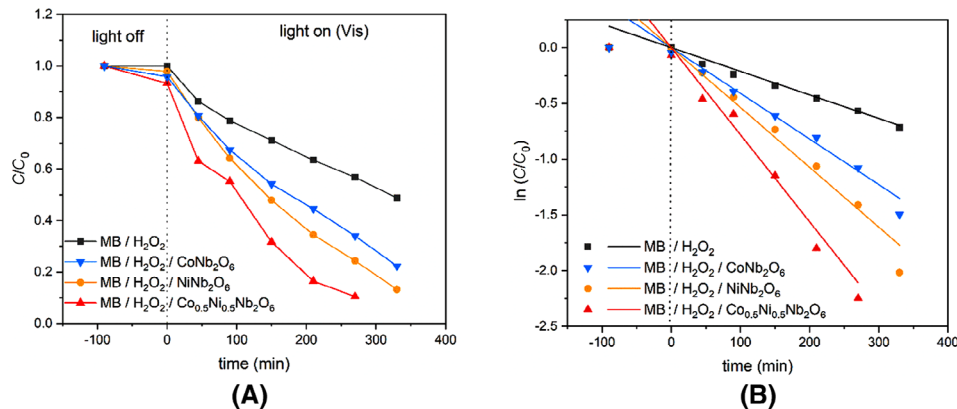


FIGURE 10 (A) The degradation efficiency of MB dye in the presence of  $\text{H}_2\text{O}_2$  and the photocatalysts under visible irradiation; (B) the first-order reaction kinetics.

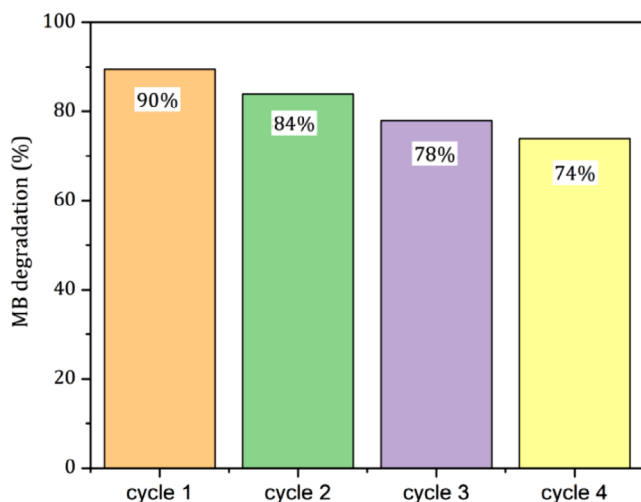
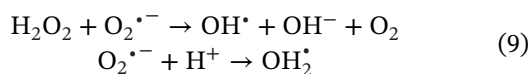
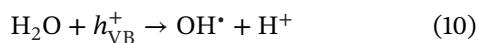


FIGURE 11 The photodegradation of MB after four cycles in the presence of the photocatalyst  $\text{Co}_{0.5}\text{Ni}_{0.5}\text{Nb}_2\text{O}_6$ .

It is possible that the  $\text{O}_2^{\bullet-}$  radicals convert to hydroperoxy ( $\text{OH}_2^{\bullet}$ ) and  $\text{OH}^{\bullet}$  radicals.



Meanwhile, the photogenerated holes react with  $\text{H}_2\text{O}$  or  $\text{HO}^-$  and form  $\text{OH}^{\bullet}$  radicals.



It should also be considered that the direct photolysis of  $\text{H}_2\text{O}_2$  and the formation of free radicals occurs after the absorption of visible light, which can be assumed to be the predominant rate-increasing mechanism in this

process<sup>107</sup>:



These generated radicals are the main active species for the degradation of the MB dye molecules by destructive oxidation process. In this way, the dual catalysts, the oxide and  $\text{H}_2\text{O}_2$  can affect the degradation of MB dye.<sup>105–107</sup> The photodegradation mechanism of MB dye on the surface of the oxides  $\text{Co}_{1-x}\text{Ni}_x\text{Nb}_2\text{O}_6$  in the presence of  $\text{H}_2\text{O}_2$  is schematically shown in Figure 12.

To confirm the proposed reaction mechanism, trapping experiments were performed to identify the main reactive species involved in the degradation of MB with  $\text{Co}_{1-x}\text{Ni}_x\text{Nb}_2\text{O}_6$  ( $x = 0, 0.5, \text{ and } 1$ ) as photocatalysts. Photodegradation was carried out in the presence of IPA, BQ and  $\text{Na}_2\text{-EDTA}$  in aqueous dye solutions during irradiation experiments, which act as quenchers for hydroxyl radicals ( $\text{OH}^{\bullet}$ ), superoxide radical anions ( $\text{O}_2^{\bullet-}$ ), and holes ( $h^+$ ), respectively.<sup>108–110</sup> All reaction conditions were the same as for the photocatalytic activity tests, with the exception of the addition of the scavenger, which was done before the catalysts were added to the solution. As can be seen in Figure 13, the addition of IPA significantly decreased the degradation of MB in the presence of  $\text{Co}_{0.5}\text{Ni}_{0.5}\text{Nb}_2\text{O}_6$ , indicating that the main active species in hydrogen-peroxide-assisted photocatalytic degradation of MB are  $\text{OH}^{\bullet}$  radicals. This is due to the fact that the hydroxyl radicals generated in the reaction mixture are immediately trapped by IPA and thus are not available for the degradation of MB.

The niobium-based columbite-type oxides found in the literature, whose photocatalytic properties for the degradation of organic dyes have been studied (Table S5),<sup>104,111–114</sup> are mainly active in the UV range, in contrast to the  $\text{Co}_{1-x}\text{Ni}_x\text{Nb}_2\text{O}_6$  oxides ( $x = 0, 0.5, \text{ and } 1$ ). This confirms that a larger average particle size reduces the energy band

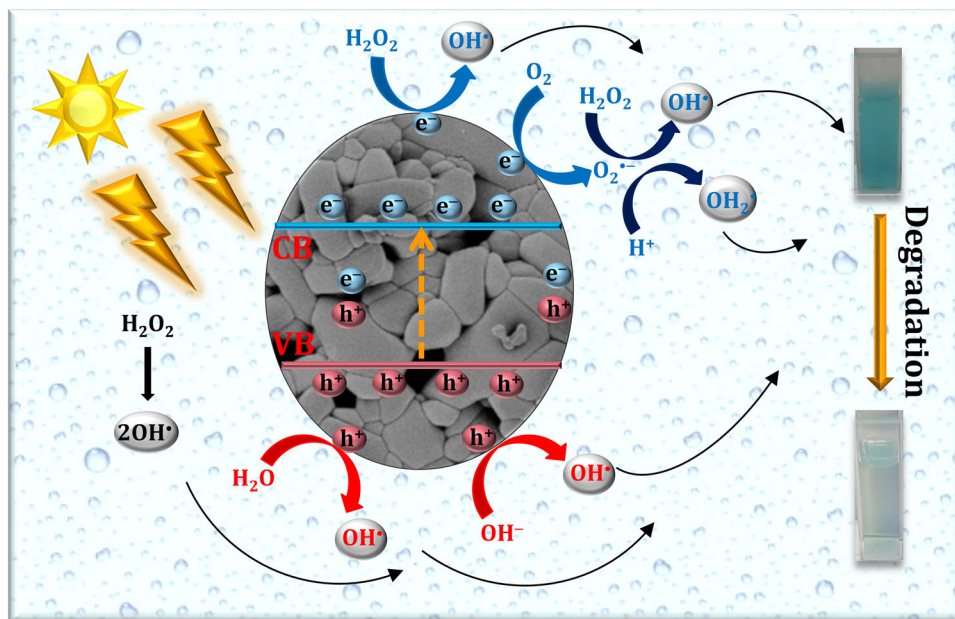


FIGURE 12 The schematic representation of the photodegradation mechanism of MB dye on the surface of  $\text{Co}_{1-x}\text{Ni}_x\text{Nb}_2\text{O}_6$  in the presence of  $\text{H}_2\text{O}_2$ .

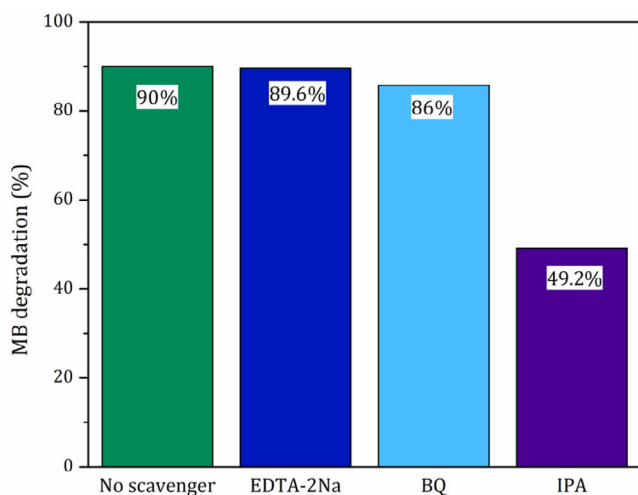


FIGURE 13 The effect of different scavengers on the MB degradation in the presence of  $\text{Co}_{0.5}\text{Ni}_{0.5}\text{Nb}_2\text{O}_6$ .

gap and thus shifts the degradation of organic dye to the visible range.<sup>103</sup> On the other hand, the larger average particle weakens the photocatalytic activity of the oxides, which must therefore be driven by  $\text{H}_2\text{O}_2$ . Recently, a 3D  $\text{NiNb}_2\text{O}_6/2\text{D E-gC}_3\text{N}_4$  type-II heterojunction was investigated as a dual catalyst for the photoreduction of  $\text{Cr}^{6+}$  to  $\text{Cr}^{3+}$  and the photo-oxidation of MB, MG, and CV under visible light. The band gap and photocatalytic activity were also investigated for pure  $\text{NiNb}_2\text{O}_6$  prepared by solid-state reaction. The photocatalytic activity was 66%, 81%, and 73% for the degradation of MB, MG, and CV, respectively, in 20 min under direct sunlight.<sup>104</sup>

Finally, it should be emphasized that the correlation between the electrical properties of a material and its photocatalytic activity is complex, but can be understood in terms of key parameters. Properties such as electrical conductivity and dielectric permittivity influence charge carrier dynamics, in particular the separation and transport of electrons and holes, which are essential for photocatalytic reactions.

The kinetic constant ( $k$ ) reflects the photodegradation rate, which is often associated with the efficiency of charge separation in the photocatalyst. A higher  $k$  value indicates faster degradation, which is associated with better charge transport properties, such as higher DC conductivity and lower activation energy for charge transfer.<sup>115</sup> The  $k_{\text{app}}$  values of the products increased from  $4.09 \times 10^{-3} \text{ min}^{-1}$  to  $7.81 \times 10^{-3} \text{ min}^{-1}$ , in the following order  $\text{Co}_{0.5}\text{Ni}_{0.5}\text{Nb}_2\text{O}_6 > \text{NiNb}_2\text{O}_6 > \text{CoNb}_2\text{O}_6$ .

Although the dielectric permittivity does not directly affect the photocatalytic process, it plays a significant role in reducing charge carrier recombination and enhancing photocatalytic efficiency.<sup>116</sup> The dielectric permittivity ( $\epsilon'$ ) indicates the ability of a material to store electrical energy in the presence of an electric field. A higher dielectric permittivity indicates that the material is more capable of polarizing in response to an external field, which improves its ability to separate and retain charge carriers. When the material is exposed to visible light, electrons from the valence band are excited to the conduction band, leaving holes behind. Efficient separation of these photogenerated electron-hole pairs is critical, as they are responsible

for driving the photocatalytic reactions. In addition, a high dielectric constant typically reduces the Coulombic attraction between the photo-generated electrons and holes, facilitating their separation and thus preventing recombination that would otherwise reduce photocatalytic efficiency.<sup>116</sup> Comparing the properties of the prepared samples (Table 3), it can be seen that  $\text{Co}_{0.5}\text{Ni}_{0.5}\text{Nb}_2\text{O}_6$  has an optimal balance between conductivity and dielectric permittivity, resulting in the best photocatalytic performance (38%). It has a high dielectric permittivity which improves the separation and mobility of charge carriers and reduces recombination, leading to greater efficiency in the degradation of dyes under visible light. In contrast,  $\text{NiNb}_2\text{O}_6$  with a slightly higher conductivity and lower permittivity, with dielectric loss in the same range ( $\sim 10^{-3}$ ) achieves a lower degradation of 35%. At the same time,  $\text{CoNb}_2\text{O}_6$  has the highest DC conductivity [ $2.64 \times 10^{-11} (\Omega \text{ cm})^{-1}$ ], but has a higher dielectric loss ( $\sim 10^{-2}$ ) and higher permittivity, which leads to a further decrease in photocatalytic performance (26% degradation). In addition, a material with a higher dielectric constant can influence its surface charge distribution, which improves the adsorption of polar molecules such as the MB dye on the catalyst surface.<sup>116</sup> Adsorption is a crucial step in the photocatalytic process as it brings the dye molecules into proximity with the photogenerated reactive species. The more efficiently the dye molecules are adsorbed, the more likely it is that they will be degraded by the reactive species formed during the photocatalytic reaction. This means that the higher the dielectric permittivity, the more efficient this process is, leading to higher degradation rates.

In general, the performance of photocatalytic systems is highly dependent on various operating parameters that control the photocatalytic degradation of the organic compounds. Some of these factors are the type of photocatalyst, morphology, crystallite size, preparation method, surface area, band gap, porosity, catalyst concentration, pH of the medium, addition of electron acceptors and donors, initial pollutant concentration, irradiation time, and light source.<sup>47,103,117</sup>

## 4 | CONCLUSIONS

In summary, we report here an unexplored approach for producing mixed metal oxides: grinding the mixture of different molecular oxalate precursors prior to thermal treatment. Our results for the preparation of columbite-type oxides,  $\text{CoNb}_2\text{O}_6$ ,  $\text{NiNb}_2\text{O}_6$ , and  $\text{Co}_{0.5}\text{Ni}_{0.5}\text{Nb}_2\text{O}_6$ , are proof of concept that binary and ternary oxides can be prepared using two or three different precursors in the appropriate ratio to ensure the desired metal composi-

tion. However, to obtain the pure phase composition, a number of parameters, including holding times, annealing temperatures, and heating and cooling rates, must be optimized. The experiments showed that controlled annealing at  $1200^\circ\text{C}$  for 10 h with a constant rate of  $10^\circ\text{C min}^{-1}$  for heating and cooling resulted in single phases with a nanocrystallite size. Moreover, to our knowledge, this is the first time an orthorhombic  $\text{Co}_{0.5}\text{Ni}_{0.5}\text{Nb}_2\text{O}_6$  phase has been prepared and characterized, and just using this modified molecular precursor route. The results confirm that the  $\text{Co}_{1-x}\text{Ni}_x\text{Nb}_2\text{O}_6$  ( $x = 0, 0.5, \text{ and } 1$ ) semiconductor nanomaterials could exhibit good photocatalytic activity for the removal of organic compounds from wastewater in the presence of  $\text{H}_2\text{O}_2$  under sunlight, as the estimated optical band gaps are 1.84–2.22 eV. The electron capturing agent plays a crucial role in controlling the recombination process at the surface, leading to a significant improvement in photocatalytic degradation activities (degradation efficiency was 26–38%). Radical trapping experiments indicate that  $\text{OH}^\bullet$  radicals play an important role during the MB degradation.

The study investigates the DC conductivity and shows a thermally activated Arrhenius-like behavior with a CBH conduction mechanism, with activation energies ranging from 0.42 to 0.69 eV. The interplay of  $\text{Co}^{2+}$  and  $\text{Ni}^{2+}$  ions significantly influenced the conductivity trend, which did not alter monotonically with composition modifications. The  $\text{CoNb}_2\text{O}_6$  has the greatest conductivity [ $2.64 \times 10^{-11} (\Omega \text{ cm})^{-1}$  at  $120^\circ\text{C}$ ], while  $\text{NiNb}_2\text{O}_6$  and  $\text{Co}_{0.5}\text{Ni}_{0.5}\text{Nb}_2\text{O}_6$  have two orders of magnitude lower values. In addition, the complex modulus formalism and impedance analysis, provided insights into non-Debye-type relaxations, emphasizing the contributions of grains and grain boundaries to charge transport, highlighting the predominant role of grain boundaries in these complex systems. This comprehensive understanding improves insight into the intricate relationship between the material composition, structural features, electrical and photocatalytic properties in these oxide systems.

## ACKNOWLEDGMENTS

This work has been funded and supported by the Croatian Science Foundation Project No. IP-2019-04-5742. The Authors acknowledge the use of SEM Thermo Fisher Scientific model Axia™ ChemiSEM™ at the Ruđer Bošković Institute delivered by the project O-ZIP (Grant Ag. No. KK.01.1.1.11.0001) cofinanced by the European Union from the European Regional Development Fund and Marija Mirosavljević for recording SEM images.

## CONFLICT OF INTEREST STATEMENT

The authors declare no conflicts of interest.

## DATA AVAILABILITY STATEMENT

The data that support the findings of this study are available from the corresponding author upon reasonable request.

## ORCID

Lidija Androš Dubraja  <https://orcid.org/0000-0002-7648-4940>

Marijana Jurić  <https://orcid.org/0000-0001-5951-9366>

## REFERENCES

- Yuan C, Wu HB, Xie YW, Lou, X. Mixed transition-metal oxides: design, synthesis, and energy-related applications. *Angew Chem Int Ed*. 2014;53:1488–504.
- Chavali MS, Nikolova MP. Metal oxide nanoparticles and their applications in nanotechnology. *SN Appl Sci*. 2019;1:607.
- Gupta SK, Mao Y. A review on molten salt synthesis of metal oxide nanomaterials: status, opportunity, and challenge. *Prog Mater Sci*. 2021;117:100734.
- Nikam AV, Prasad BLV, Kulkarni AA. Wet chemical synthesis of metal oxide nanoparticles: a review. *CrystEngComm*. 2018;20:5091–107.
- Parashar M, Shukla VK, Singh R. Metal oxides nanoparticles via sol–gel method: a review on synthesis, characterization and applications. *J Mater Sci: Mater Electron*. 2020;31:3729–3749.
- Yin Z, Li S, Li X, Shi W, Liu W, Gao Z, et al. A review on the synthesis of metal oxide nanomaterials by microwave induced solution combustion. *RSC Adv*. 2023;13:3265–77.
- Guo T, Yao M-S, Lin Y-H, Nan C-W. A comprehensive review on synthesis methods for transition-metal oxide nanostructures. *CrystEngComm*. 2015;17:3551–3585.
- Nunes GG, Seisenbaeva GA, Kessler VG. Crystal engineering of nanomorphology for complex oxide materials via thermal decomposition of metal–organic frameworks. Case study of sodium tantalate. *Cryst Growth Des*. 2011;11:1238–43.
- Bayot D, Tinant B, Devillers M. Homo- and heterobimetallic niobium<sup>v</sup> and tantalum<sup>v</sup> peroxo-tartrate complexes and their use as molecular precursors for Nb–Ta mixed oxides. *Inorg Chem*. 2005;44:1554–62.
- Thurston JH, Whitmire KH. Molecular precursors for ferroelectric materials: synthesis and characterization of Bi<sub>2</sub>M<sub>2</sub>(μ-O)(sal)<sub>4</sub>(Hsal)<sub>4</sub>(OEt)<sub>2</sub> and BiM<sub>4</sub>(μ-O)<sub>4</sub>(sal)<sub>4</sub>(Hsal)<sub>3</sub>(O<sup>i</sup>Pr)<sub>4</sub> (sal = O<sub>2</sub>CC<sub>6</sub>H<sub>4</sub>O, Hsal = O<sub>2</sub>CC<sub>6</sub>H<sub>4</sub>OH) (M = Nb, Ta). *Inorg Chem*. 2003;42:2014–23.
- Thurston JH, Whitmire KH. Heterobimetallic bismuth–transition metal salicylate complexes as molecular precursors for ferroelectric materials. Synthesis and structure of Bi<sub>2</sub>M<sub>2</sub>(sal)<sub>4</sub>(Hsal)<sub>4</sub>(OR)<sub>4</sub> (M = Nb, Ta; R = CH<sub>2</sub>CH<sub>3</sub>, CH(CH<sub>3</sub>)<sub>2</sub>), Bi<sub>2</sub>Ti<sub>3</sub>(sal)<sub>8</sub>(Hsal)<sub>2</sub>, and Bi<sub>2</sub>Ti<sub>4</sub>(O<sup>i</sup>Pr)(sal)<sub>10</sub>(Hsal) (sal = O<sub>2</sub>CC<sub>6</sub>H<sub>4</sub>-2-O; Hsal = O<sub>2</sub>CC<sub>6</sub>H<sub>4</sub>-2-OH). *Inorg Chem*. 2002;41:4194–205.
- Lu H, Wright DS, Pike SD. The use of mixed-metal single source precursors for the synthesis of complex metal oxides. *Chem Commun*. 2020;56:854–71.
- Barry MC, Wei Z, He T, Filatov AS, Dikarev EV. Volatile single-source precursors for the low-temperature preparation of sodium–rare earth metal fluorides. *J Am Chem Soc*. 2016;138:8883–87.
- Navulla A, Huynh L, Wei ZA, Filatov S, Dikarev EV. Volatile single-source molecular precursor for the lithium ion battery cathode. *J Am Chem Soc*. 2012;134:5762–65.
- Li M, Yang K, Liu J, Hu X, Kong D, Liu T, et al. A heterobimetallic single-source precursor enabled layered oxide cathode for sodium-ion batteries. *Chem Commun*. 2018;54:10714–17.
- Li M, Liu J, Liu T, Zhang M, Pan F. A versatile single molecular precursor for the synthesis of layered oxide cathode materials for Li-ion batteries. *Chem Commun*. 2018;54:1331–34.
- Han H, Wei Z, Barry MC, Filatov AS, Dikarev EV. Heterometallic molecular precursors for lithium-iron oxide material: synthesis, solid state structure, solution and gas-phase behaviour, and thermal decomposition. *Dalton Trans*. 2017;46:5644–49.
- Neo KE, Ong YY, Huynh HV, Hor TSA. A single-molecular pathway from heterometallic MM' (M = Ba<sup>II</sup>, Mn<sup>II</sup>; M' = Cr<sup>III</sup>) oxalate complexes to intermetallic composite oxides. *J Mater Chem*. 2007;17:1002–6.
- Coronado E, Marti-Gastaldo C, Galañ-Mascarós JR, Cavallini M. Polymetallic oxalate-based 2D magnets: soluble molecular precursors for the nanostructuring of magnetic oxides. *J Am Chem Soc*. 2010;132:5456–68.
- Guo L, Arafune H, Teramae N. Synthesis of mesoporous metal oxide by the thermal decomposition of oxalate precursor. *Langmuir*. 2013;29:4404–12.
- Wada S, Narahara M, Hoshina T, Kakemoto H, Tsurumi T. Preparation of nm-sized BaTiO<sub>3</sub> particles using a new 2-step thermal decomposition of barium titanate oxalate. *J Mater Sci*. 2003;38:2655–60.
- Habjanić J, Jurić M, Popović J, Molčanov K, Pajić D. A 3D oxalate-based network as a precursor for the CoMn<sub>2</sub>O<sub>4</sub> spinel: synthesis and structural and magnetic studies. *Inorg Chem*. 2014;53:9633–43.
- Popović J, Jurić M, Pajić D, Vrankić M, Zavašnik J, Habjanić J. Effect of the cation distribution and microstructure on the magnetic behavior of the CoMn<sub>2</sub>O<sub>4</sub> oxide. *Inorg Chem*. 2017;56:3983–89.
- Jurić M, Pajić D, Žilić D, Rakvin B, Molčanov K, Popović J. Magnetic order in a novel 3D oxalate-based coordination polymer {[Cu(bpy)]<sub>3</sub>[Mn<sub>2</sub>(C<sub>2</sub>O<sub>4</sub>)<sub>3</sub>]·H<sub>2</sub>O}<sub>n</sub>. *Dalton Trans*. 2015;44:20626–35.
- Jurić M, Popović J, Šantić A, Molčanov K, Brničević N, Planinić P. Single-step preparation of the mixed Ba<sup>II</sup>–Nb<sup>V</sup> oxides from a heteropolynuclear oxalate complex. *Inorg Chem*. 2013;52:1832–42.
- Androš L, Jurić M, Popović J, Šantić A, Lazić P, Benčina M, et al. Ba<sub>4</sub>Ta<sub>2</sub>O<sub>9</sub> oxide prepared from an oxalate-based molecular precursor—characterization and properties. *Inorg Chem*. 2013;52:14299–308.
- Popović J, Vrankić M, Jurić M. Tuning the microstructure of γ-Ba<sub>4</sub>Nb<sub>2</sub>O<sub>9</sub> polymorph prepared from single-molecular precursor. *Cryst Growth Des*. 2013;13:2161–65.
- Androš L, Jurić M, Popović J, Pajić D, Zadro K, Molčanov K, et al. 1D heterometallic oxalate compounds as precursors for mixed Ca–Cr oxides—synthesis, structures, and magnetic studies. *Eur J Inorg Chem*. 2014:5703–13.
- Androš Dubraja L, Pajić D, Vrankić M, Dragović J, Valant M, Benčina M, et al. Single-step preparation of rutile-type CrNbO<sub>4</sub>

- and CrTaO<sub>4</sub> oxides from oxalate precursors—characterization and properties. *J Am Ceram Soc.* 2019;102:6697–704.
30. Molčanov L, Androš Dubraja L, Vrankić M, Jurić M. A 3D oxalate-bridged [Cu<sup>II</sup>Fe<sup>II</sup>] coordination polymer as molecular precursor for CuFe<sub>2</sub>O<sub>4</sub> spinel—photocatalytic features. *J Am Ceram Soc.* 2023;106:2997–3008.
  31. Thurston JH, Ely TO, Trahan D, Whitmire KH. Nanostructured bimetallic oxide ion-conducting ceramics from single-source molecular precursors. *Chem Mater.* 2003;15:4407–16.
  32. Lei S, Wang C, Guo D, Gao X, Cheng D, Zhou J, et al. Synthesis and magnetic properties of MNb<sub>2</sub>O<sub>6</sub> (M = Fe, Co, Ni) nanoparticles. *RSC Adv.* 2014;4:52740–48.
  33. Heid C, Weitzel H, Burlet P, Winkelmann M, Ehrenberg H, Fuess H. Magnetic phase diagrams of CoNb<sub>2</sub>O<sub>6</sub>. *Phys B* 1997;234–236:574–75.
  34. Heid C, Weitzel H, Burlet P, Bonnet M, Gonschorek W, Vogt T, et al. Magnetic phase diagram of CoNb<sub>2</sub>O<sub>6</sub>: a neutron diffraction study. *J Magn Magn Mater* 1995;151:123–31.
  35. Pullar RC. The synthesis, properties, and applications of columbite niobates (M<sup>2+</sup>Nb<sub>2</sub>O<sub>6</sub>): a critical review. *J Am Ceram Soc* 2009;92:563–77.
  36. Heid C, Weitzel H, Bourdarot F, Calemczuk R, Vogt T, Fuess H. Magnetism in FeNb<sub>2</sub>O<sub>6</sub> and NiNb<sub>2</sub>O<sub>6</sub>. *J Phys Condens Matter.* 1996;8:10609–25.
  37. Sarvezuk PWC, Kinast EJ, Colin CV, Gusmão MA, da Cunha JBM, Isnard O. New investigation of the magnetic structure of CoNb<sub>2</sub>O<sub>6</sub> columbite. *J Appl Phys.* 2011;109:07E160.
  38. De Luna Y, Bensalah N. Mechanochemical synthesis of orthorhombic nickel niobate (NiNb<sub>2</sub>O<sub>6</sub>) as a robust and fast charging anode material for lithium-ion batteries. *ACS Appl Energy Mater.* 2022;5:7443–57.
  39. Zhao S, Lian J, Zhang S, Cui Y, Li G, Wang Y, et al. Molten salt synthesis of submicron NiNb<sub>2</sub>O<sub>6</sub> anode material with ultrahigh rate performance for lithium-ion batteries. *Chem Eng J.* 2023;461:141997.
  40. Martínez-de la Cruz A, Alcaraz NL, Fuentes AF, Torres-Martínez LM. Electrochemical lithium insertion in some niobates MNb<sub>2</sub>O<sub>6</sub> (M = Mn, Co, Ni, Cu, Zn and Cd). *J Power Sources.* 1999;81–82:255–58.
  41. Zhou YY, Lu MK, Qiu ZF, Zhang AY, Ma Q, Zhang HP, et al. Photoluminescence of NiNb<sub>2</sub>O<sub>6</sub> nanoparticles prepared by combustion method. *Mater Sci Eng B.* 2007;140:128–31.
  42. Ye JH, Zou ZG, Matsushita A. A novel series of water splitting photocatalysts NiM<sub>2</sub>O<sub>6</sub> (M = Nb; Ta) active under visible light. *Int J Hydrogen Energy.* 2003;28:651–55.
  43. Samuel V, Gaikwad AB, Jadhav AD, Natarajan N, Ravi V. A coprecipitation technique to prepare NiNb<sub>2</sub>O<sub>6</sub>. *Mater Lett.* 2007;61:2354–55.
  44. Mulla IS, Natarajan N, Gaikwad AB, Samuel V, Guptha UN, Ravi V. A coprecipitation technique to prepare CoTa<sub>2</sub>O<sub>6</sub> and CoNb<sub>2</sub>O<sub>6</sub>. *Mater Lett.* 2007;61:2127–29.
  45. Ma R, Cao F, Wang J, Zhu G, Pang G. Hydrothermal synthesis and phase stability of CoNb<sub>2</sub>O<sub>6</sub> with a rutile structure. *Mater Lett.* 2011;65:2880–82.
  46. Dippong T, Levei EA, Cadar O. Recent advances in synthesis and applications of MFe<sub>2</sub>O<sub>4</sub> (M = Co, Cu, Mn, Ni, Zn) nanoparticles. *Nanomaterials.* 2021;11:1560.
  47. Kirankumar VS, Sumathi S. A review on photodegradation of organic pollutants using spinel oxide. *Mater Today Chem.* 2020;18:100355.
  48. Jurić M, Perić B, Brničević N, Planinić P, Pajić D, Zadro K, et al. Supramolecular motifs and solvatomorphism within the compounds [M(bpy)<sub>3</sub>]<sub>2</sub>[NbO(C<sub>2</sub>O<sub>4</sub>)<sub>3</sub>]Cl·nH<sub>2</sub>O (M = Fe<sup>2+</sup>, Co<sup>2+</sup>, Ni<sup>2+</sup>, Cu<sup>2+</sup> and Zn<sup>2+</sup>; n = 11, 12). Syntheses, structures and magnetic properties. *Dalton Trans.* 2008:742–54.
  49. Rietveld HM. A profile refinement method for nuclear and magnetic structures. *J Appl Crystallogr.* 1969;2:65–71.
  50. X'Pert highscore plus program, ver. 4.1. Almelo, Netherlands: PANalytical B. V. 2014.
  51. Caglioti G, Paoletti A, Ricci FP. Choice of collimators for a crystal spectrometer for neutron diffraction. *Nucl Instrum Methods.* 1958;3:223–28.
  52. Tauc J, Grigorovici R, Vancu A. Optical properties and electronic structure of amorphous germanium. *Phys Status Solidi B.* 1996;15:627–37.
  53. Vrankić M, Šarić A, Nakagawa T, Ding Y, Despotović I, Kanižaj L, et al. Pressure-induced and flaring photocatalytic diversity of ZnO particles hallmarked by finely tuned pathways. *J Alloys Compd.* 2021;894:162444.
  54. WinFIT software, version 3.2. Hundsangen, Germany: Novocontrol Technologies GmbH & Co. KG.
  55. Ko EI, Weissman JG. Structures of niobium pentoxide and their implications on chemical behaviour. *Catal Today.* 1990;8:27–36.
  56. de M. Gomes GH, de Andrade RR, Mohallem NDS. Investigation of phase transition employing strain mapping in TT- and T-Nb<sub>2</sub>O<sub>5</sub> obtained by HRTEM micrographs. *Micron.* 2021;148:103112.
  57. Pang R, Wang Z, Li J, Chen K. Polymorphs of Nb<sub>2</sub>O<sub>5</sub> compound and their electrical energy storage applications. *Materials.* 2023;16:6956.
  58. Weissman JG, Ko EI, Wynblatt P, Howe JM. High-resolution electron microscopy and image simulation of TT-, T-, and H-niobia and model silica-supported niobium surface oxides. *Chem Mater.* 1989;1:187–93.
  59. Rooksby H, Hinatsu Y, Nishimine H. Structure of nickel oxide. *Nature.* 1943;152:304.
  60. Wichmann R, Mueller-Buschbaum HK. Synthese und Untersuchung von NiNb<sub>2</sub>O<sub>6</sub>-Einkristallen mit Columbit—und Rutilstruktur. *Z Anorg Allg Chem.* 1983;503:101–5.
  61. Ehrenberg H, Wltschek G, Weitzel H, Trouw F, Buettner JH, Kroener T, et al. Ferrimagnetism in Ni<sub>4</sub>Nb<sub>2</sub>O<sub>9</sub>. *Phys Rev B Condens.* 1995;52:9595–600.
  62. Gomes GHM, Mohallem NDS. CSD 2103847: experimental crystal structure determination. 2021. <https://doi.org/10.25505/iz.icsd.cc28m716>
  63. Gomes GHM, Mohallem NDS. Insights into the TT-Nb<sub>2</sub>O<sub>5</sub> crystal structure behaviour. *Mater Lett.* 2022;318:132136.
  64. Abidin SZ, Ling GKF, C Abdullah L, Ahmad S, Yunus R, Choong TSY. Effects of temperature and cooling modes on yield, purity and particle size distribution of dihydroxystearic acid crystals. *Eur J Sci Res.* 2009;33:471–79.
  65. Stichert W, Schüth F. Influence of crystallite size on the properties of zirconia. *Chem Mater.* 1998;10:2020–26.
  66. Kashiwaya Y, Cicutti CE, Cramb AW. An investigation of the crystallization of a continuous casting mold slag using the single hot thermocouple technique. *ISIJ Int.* 1998;38:357–65.
  67. Guo J, Seo MD, Shi CB, Cho JW, Kim SH. Control of crystal morphology for mold flux during high-aluminum AHSS continuous casting process. *Metall Mater Trans B.* 2016;47B:2211–21.

68. Leng M, Lai F, Li J. Effect of cooling rate on phase and crystal morphology transitions of CaO–SiO<sub>2</sub>-based systems and CaO–Al<sub>2</sub>O<sub>3</sub>-based systems. *Materials*. 2019;12:62.
69. Li J, Lai F, Yao W, Hu L, Liu Q. Effects of the cooling rate on the crystallization behaviors of the CaO–Al<sub>2</sub>O<sub>3</sub>–B<sub>2</sub>O<sub>3</sub>–CaF<sub>2</sub>-based mold flux. *CrystEngComm*. 2020;22:2158–65.
70. Krupiński M, Krupińska B, Labisz K, Rdzawski Z, Borek W. Influence of cooling rate on crystallisation kinetics on microstructure of cast zinc alloys. *J Therm Anal Calorim*. 2014;118:1361–67.
71. Ngamjarujana A, Khamman O, Yimnirun R, Ananta S. Effect of calcination conditions on phase formation and particle size of zinc niobate powders synthesized by solid-state reaction. *Mater Lett*. 2006;60:2867–72.
72. Reed JS. *Principles of ceramic processing*. 2nd ed. New York: Wiley; 1995.
73. Weitzel H. Kristallstrukturverfeinerung von Wolframiten und Columbiten. *Z Kristallogr Krist*. 1976;144:238–58.
74. Maruthi R, Deshpande SK, Deshmukh V, Singh K, Thota S. Correlated barrier charge hopping and non-Debye relaxation in columbite MnNb<sub>2</sub>O<sub>6</sub>. *J Phys D Appl Phys*. 2023;56:025501.
75. Singh KN, Bajpai PK. Synthesis, characterization and dielectric relaxation of phase pure columbite MgNb<sub>2</sub>O<sub>6</sub>: optimization of calcination and sintering. *Phys B Condens Matter*. 2010;405:303–12.
76. Thakur S, Rai R, Bdkin I, Valente MA. Impedance and modulus spectroscopy characterization of Tb modified Bi<sub>0.8</sub>A<sub>0.1</sub>Pb<sub>0.1</sub>Fe<sub>0.9</sub>Ti<sub>0.1</sub>O<sub>3</sub> ceramics. *Mater Res*. 2016;19:1–8.
77. Lee H-J, Hong K-S, Kim S-J, Kim I-T. Dielectric properties of MNb<sub>2</sub>O<sub>6</sub> compounds (where M = Ca, Mn, Co, Ni, or Zn). *Mater Res Bull* 1997;32:847–55.
78. Hizi W, Rahmouni H, Gassoumi M, Khirouni K, Dhahri S. Transport properties of La<sub>0.9</sub>Sr<sub>0.1</sub>MnO<sub>3</sub> manganite. *Eur Phys J Plus*. 2020;135:1–13.
79. Mondal T, Das S, Sinha TP, Sarun PM. Dielectric relaxation and study of electrical conduction mechanism in BaZr<sub>0.1</sub>Ti<sub>0.9</sub>O<sub>3</sub> ceramics by correlated barrier hopping model. *Mater Sci-Pol*. 2018;36:112–22.
80. Javed M, Khan AA, Ahmed MS, Khisro SN, JK MS, Bilkees R, et al. Temperature dependent impedance spectroscopy and electrical transport mechanism in sol-gel derived MgCr<sub>2</sub>O<sub>4</sub> spinel oxide. *Phys B Condens Matter*. 2020;599:412377.
81. Singh KN, Parmendra KB. Dielectric relaxation in pure columbite phase of SrNb<sub>2</sub>O<sub>6</sub> ceramic material: impedance analysis. *World J Condens Matter Phys*. 2011;1:37.
82. Ang C, Yu Z, Cross LE. Oxygen-vacancy-related low-frequency dielectric relaxation and electrical conduction in Bi: SrTiO<sub>3</sub>. *Phys Rev B*. 2000;62:228.
83. Abdouli K, Hassini F, Cherif W, Prezas PR, Graça, MPP, Valent MA, et al. Investigation of the structural, electrical, and dielectric properties of La<sub>0.5</sub>Sm<sub>0.2</sub>Sr<sub>0.3</sub>Mn<sub>1-x</sub>Cr<sub>x</sub>O<sub>3</sub> for electrical application. *RSC Adv*. 2022;12:16805–22.
84. Shukla A, Choudhary RNP, Thakur AK. Effect of Mn<sup>4+</sup> substitution on thermal, structural, dielectric and impedance properties of lead titanate. *J Mater Sci: Mater Electron*. 2009;20:745–755.
85. Irvine JT, Sinclair DC, West AR. *Electroceramics: characterization by impedance spectroscopy*. *Adv Mater* 1990;2:132–38.
86. Sinclair DC. Characterisation of electro-materials using AC impedance spectroscopy. *Bol Soc Esp Cerám Vidrio* 1995;34:55–65.
87. Belous AG, Ovchar OV, Kramarenko AV, Mishchuk DO, Jancar B, Bezjak J, et al. Effect of nonstoichiometry on the structure and microwave dielectric properties of cobalt metaniobate. *Inorg Mater*. 2006;42:1369–73.
88. Pullar RC, Breeze JD, Alford NM. Characterization and microwave dielectric properties of M<sup>2+</sup>Nb<sub>2</sub>O<sub>6</sub> ceramics. *J Am Ceram Soc*. 2005;88:2466–71.
89. Kang Y, Jeon D, Kim T. Local mapping of the thickness-dependent dielectric constant of MoS<sub>2</sub>. *J Phys Chem C*. 2021;125:3611–15.
90. Zurich Instruments AG. *Measuring dielectric properties of materials with varying thickness*. Zurich: Zurich Instruments; 2021. <https://www.zhinst.com/europe/en/blogs/measuring-dielectric-properties-materials-varying-thickness>
91. Singh N, Ashish A, Sujata S, Khasa S. Dielectric loss, conductivity relaxation process and magnetic properties of Mg substituted Ni–Cu ferrites. *J Magn Magn Mater*. 2012;324:2506–11.
92. Lever ABP. *Inorganic electronic spectroscopy*. Amsterdam: Elsevier; 1968.
93. Arroyo y de Dompablo ME, Lee Y-L, Morgan D. First principles investigation of oxygen vacancies in columbite MNb<sub>2</sub>O<sub>6</sub> (M = Mn, Fe, Co, Ni, Cu). *Chem Mater*. 2010;22:906–13.
94. Molla K, Rahaman B. Electronic structure and microscopic model of CoNb<sub>2</sub>O<sub>6</sub>. *AIP Conf Proc*. 2018;1953:120011.
95. Balamurugan C, Maheswari AR, Lee D-W. Structural, optical, and selective ethanol sensing properties of p-type semiconducting CoNb<sub>2</sub>O<sub>6</sub> nanopowder. *Sens Actuators B Chem*. 2014;205:289–97.
96. Jones BMF, Mamba G, Ansari SA, Maruthamani D, Muthuraj V, Nkambule TTI. Simple fabrication and unprecedented visible light response of NiNb<sub>2</sub>O<sub>6</sub>/RGO heterojunctions for the degradation of emerging pollutants in water. *New J Chem*. 2021;45:22697–713.
97. Nasrollahzadeh M, Sajjadi M, Irvani S, Varma RS. Green-synthesized nanocatalysts and nanomaterials for water treatment: current challenges and future perspectives. *J Hazard Mater*. 2021;401:123401.
98. Khan S, Noor T, Iqbal N, Yaqoob L. Photocatalytic dye degradation from textile wastewater: a review. *ACS Omega*. 2024;9:21751–67.
99. Krishnan A., Swarnalal A, Das D, Krishnan M, Saji VS, Shibli SMA. A review on transition metal oxides based photocatalysts for degradation of synthetic organic pollutants. *J Environ Sci*. 2024;139:389–417.
100. Kudo A, Miseki Y. Heterogeneous photocatalyst materials for water splitting. *Chem Soc Rev*. 2009;38:253–78.
101. Tee SY, Win KY, Teo WS, Koh L-D, Liu S, Teng CP, et al. Recent progress in energy-driven water splitting. *Adv Sci*. 2017;4:1600337.
102. Kong D, Zheng Y, Kobielski M, Wang Y, Bai Z, Macyk W, et al. Recent advances in visible light-driven water oxidation and reduction in suspension systems. *Mater Today*. 2018;21:897–924.
103. Khatun M, Mitra P, Mukherjee S. Effect of band gap and particle size on photocatalytic degradation of NiSnO<sub>3</sub> nanopowder for some conventional organic dyes. *Hybrid Adv*. 2023;4:100079.

104. Arulprakash G, Vijayaraghavan R. Charge-separated 3D/2D layered heterojunction of  $\text{NiNb}_2\text{O}_6/\text{E-gC}_3\text{N}_4$  as an efficient photocatalyst for photo-reduction of  $\text{Cr}^{6+}$  and photo-oxidation of dyes under visible and sunlight. *Appl Surf Sci.* 2025;684:161938.
105. Resende SF, Augusti R, de Lima GM, Gouveia RL, Oliveira BS, Krambrock K, et al. Visible-light driven catalytic activity of two novel Cu(II) and Ni(II) titanium niobates. *J Environ Chem Eng.* 2019;7:103065.
106. Waimbo M, Anduwana G, Renagi O, Badhula S, Michael K, Park J, et al. Improved charge separation through  $\text{H}_2\text{O}_2$  assisted copper tungstate for enhanced photocatalytic efficiency for the degradation of organic dyes under simulated sun light. *J Photochem Photobiol B Biol.* 2020;204:111781.
107. Tantubay K, Das P, Baskey (Sen) M. Hydrogen peroxide-assisted photocatalytic dye degradation over reduced graphene oxide integrated  $\text{ZnCr}_2\text{O}_4$  nanoparticles. *Environ Sci Pollut Res.* 2022;29:17309–18.
108. Alam U, Kumar S, Bahnemann D, Koch J, Tegenkamp D, Muneer M. Harvesting visible light with  $\text{MoO}_3$  nanorods modified by Fe(III) nanoclusters for effective photocatalytic degradation of organic pollutants. *Phys Chem Chem Phys.* 2018;20:4538–45.
109. Li F, Wang Y, Wang K, Zhang L, Han G, Ye M, et al. Enhanced photocatalytic degradation of tetracycline by a  $\text{H}_2\text{O}_2$ -assisted  $\text{Bi}_3\text{NbO}_7/\text{Bi}_2\text{Sn}_2\text{O}_7$  composite under visible light. *Phys Chem Chem Phys.* 2023;25:4553–62.
110. Alam U, Khan A, Ali D, Bahnemann D, Muneer M. Comparative photocatalytic activity of sol-gel derived rare earth metal (La, Nd, Sm and Dy)-doped ZnO photocatalysts for degradation of dyes. *RSC Adv.* 2018;8:17582–94.
111. Cho IS, Kim DW, Cho CM, An JS, Roh HS, Hong KS. Synthesis, characterization and photocatalytic properties of  $\text{CaNb}_2\text{O}_6$  with ellipsoid-like plate morphology. *Solid State Sci.* 2010;12:982–88.
112. Huang X, Jing Y, Yang J, Ju J, Cong R, Gao W, et al. Flower-like nanostructure  $\text{MNb}_2\text{O}_6$  ( $\text{M} = \text{Mn, Zn}$ ) with high surface area: hydrothermal synthesis and enhanced photocatalytic performance. *Mater Res Bull.* 2014;51:271–76.
113. Basavaraju N, Raghavendra N, Hamdalla TA, Ravikumar CR, Nagaswarupa HP, Shekhar TRS, et al. A novel synthesis of  $\text{ZnNb}_2\text{O}_6$  nanoparticles via combustion method: supercapacitor and photocatalytic properties. *Part Part Syst Charact.* 2024;41:2400061.
114. Basavaraju N, Prashantha SC, Surendra BS, Shekhar TRS, Kumar MRA, Ravikumar CR, et al. Structural and optical properties of  $\text{MgNb}_2\text{O}_6$  NPs: its potential application in photocatalytic and pharmaceutical industries as sensor. *Environ Nanotechnol Monit Manag.* 2021;16:100581.
115. Coronado JM, Fresno F, Hernández-Alonso MD, Portela R, editors. Design of advanced photocatalytic materials for energy and environmental applications. Vol. 71. London: Springer; 2013.
116. Chen F, Ma T, Zhang T, Zhang Y, Huang H. Atomic-level charge separation strategies in semiconductor-based photocatalysts. *Adv Mater.* 2021;33:2005256.
117. Shah P, Unnarkat A, Patel F, Shah M, Shah P. A comprehensive review on spinel based novel catalysts for visible light assisted dye degradation. *Process Saf Environ Prot.* 2022;161:703–22.

## SUPPORTING INFORMATION

Additional supporting information can be found online in the Supporting Information section at the end of this article.

**How to cite this article:** Lozančić A, Vrankić M, Razum M, Pavić L, Androš Dubraja L, Jurić M. Molecular precursor pathway to  $\text{Co}_{1-x}\text{Ni}_x\text{Nb}_2\text{O}_6$  for photocatalytic dye degradation: Optical and charge transport studies. *J Am Ceram Soc.* 2025;108:e20485. <https://doi.org/10.1111/jace.20485>